9

Review article

Dmitri V. Voronine*, Zhenrong Zhang, Alexei V. Sokolov and Marlan O. Scully

Surface-enhanced FAST CARS: en route to quantum nano-biophotonics

https://doi.org/10.1515/nanoph-2017-0066 Received July 1, 2017; revised September 7, 2017; accepted September 15, 2017

Abstract: Quantum nano-biophotonics as the science of nanoscale light-matter interactions in biological systems requires developing new spectroscopic tools for addressing the challenges of detecting and disentangling weak congested optical signals. Nanoscale bio-imaging addresses the challenge of the detection of weak resonant signals from a few target biomolecules in the presence of the nonresonant background from many undesired molecules. In addition, the imaging must be performed rapidly to capture the dynamics of biological processes in living cells and tissues. Label-free non-invasive spectroscopic techniques are required to minimize the external perturbation effects on biological systems. Various approaches were developed to satisfy these requirements by increasing the selectivity and sensitivity of biomolecular detection. Coherent anti-Stokes Raman scattering (CARS) and surface-enhanced Raman scattering (SERS) spectroscopies provide many orders of magnitude enhancement of chemically specific Raman signals. Femtosecond adaptive spectroscopic techniques for CARS (FAST CARS) were developed to suppress the nonresonant background and optimize the efficiency of the coherent optical signals. This perspective focuses on the application of these techniques to nanoscale bioimaging, discussing their advantages and limitations as well as the promising opportunities and challenges of the combined coherence and surface enhancements in surface-enhanced coherent anti-Stokes Raman scattering (SECARS) and tip-enhanced coherent anti-Stokes Raman scattering (TECARS) and the corresponding surfaceenhanced FAST CARS techniques. Laser pulse shaping of near-field excitations plays an important role in achieving these goals and increasing the signal enhancement.

*Corresponding author: Dmitri V. Voronine, Department of Physics, University of South Florida, Tampa, FL 33620, USA, e-mail: dmitri. voronine@gmail.com. http://orcid.org/0000-0002-8841-7657

Zhenrong Zhang: Baylor University, Waco, TX 76798, USA

Alexei V. Sokolov and Marlan O. Scully: Baylor University,

Waco, TX 76798, USA; and Texas A&M University, College Station,

TX 77843, USA

Keywords: FAST CARS; laser pulse shaping; nanoantenna; quantum biophotonics; SECARS; TECARS.

1 Introduction

At the interface between quantum optics and biophysics lies the emerging exciting field of quantum biophotonics [1]. With new light sources and quantum effects, it is becoming increasingly possible to apply the techniques of quantum spectroscopy to biosciences. A new paradigm shift has been emerging in which the biologists define the parameters that are needed for effective use, and the quantum physicists/engineers design and develop the technology to meet those needs. For example, recent exciting developments of new radiation sources improved the detection of trace impurities via quantum coherence, and related effects improved microscopic resolution (Nobel Prize, 2014). Quantum limits of the existing classical techniques, such as the quantum plasmonic effects in surfaceenhanced sensing, have been identified. New technological breakthroughs are needed to address the remaining challenges of nanoscale label-free rapid bio-imaging, with the ultimate goal of obtaining ultrafast molecular movies in living organisms. This requires developing new techniques and pushing the envelope in quantum physics on the one hand and bioscience on the other. In this review, we describe recent progress in surface-enhanced coherent Raman spectroscopy and give a perspective on the use of near-field laser pulse shaping to optimize this technique.

2 Femtosecond adaptive spectroscopic techniques for coherent anti-Stokes Raman scattering (FAST CARS)

Chemically specific optical imaging and sensing techniques play a pivotal role in developing preventive measures to maintain chemical and biological safety and in

biomedical imaging. The detection of a chemically specific target in a harsh and complex environment presents several problems. First, a small number of targeted molecules are not directly accessible for interrogation and yield weak optical signals. On passing through the scattering biological medium, both the incident light and the optical signal are substantially diminished, weakening the signal and diffusing the spatial information about the signal's origin. Second, the chemical specificity has to be maintained in the presence of a substantial background from the surrounding chemicals.

Laser spectroscopy has been widely used for the chemical analysis of living systems. For example, Raman and infrared (IR) spectroscopies can probe the vibrational states of molecules in order to determine, for example, the chemical assay and temperature profile. IR spectroscopy is widely used because it is simple and inexpensive. The major drawback is the high absorption of water in IR. Raman spectroscopy is more complicated but has many advantages and is a more versatile and powerful tool. The major drawback of spontaneous Raman spectroscopy is the weak signal strength. Coherent and stimulated Raman techniques can be used to increase the speed and strength of the imaging signal acquisition by orders of magnitude [2–6]. For example, in the CARS spectroscopy, the signal is proportional to the number of molecules squared as opposed to the linear dependence in the spontaneous Raman technique [7]. However, the nonresonant background also makes a significant contribution.

We have developed a new FAST CARS based on optimal laser pulse shaping for background suppression and demonstrated the first application to the precision sensing of minor molecular species within a highly scattering environment [8], and we also provided a very efficient solution to the problem of detecting and identifying anthrax-type bacterial endospores in real time [9, 10]. Figure 1 shows the basic idea behind the FAST CARS approach. In the case of conventional CARS (Figure 1A and C), two lasers with frequencies $\omega_{\rm p}$ and $\omega_{\rm s}$ (referred to as lasers 1 and 2, respectively) are incident on a sample. When the difference frequency is resonant with some molecular vibration at $\Omega_{\mbox{\tiny p}}$, the sample may also absorb a third photon (either a third laser with frequency ω_{pr} or a second photon from laser 1, $\omega_{\rm p} = \omega_{\rm pr}$) and generate light at frequency $\omega_{\text{sig}} = \omega_{\text{p}} - \omega_{\text{s}} + \omega_{\text{pr}}$.

The problem is that the process is masked by the nonresonant four-wave mixing (FWM) background that produces broadband nonlinear generation that can be much larger than the vibrationally resonant CARS signal. FAST CARS was developed for suppressing the nonresonant background based on laser pulse shaping and is shown

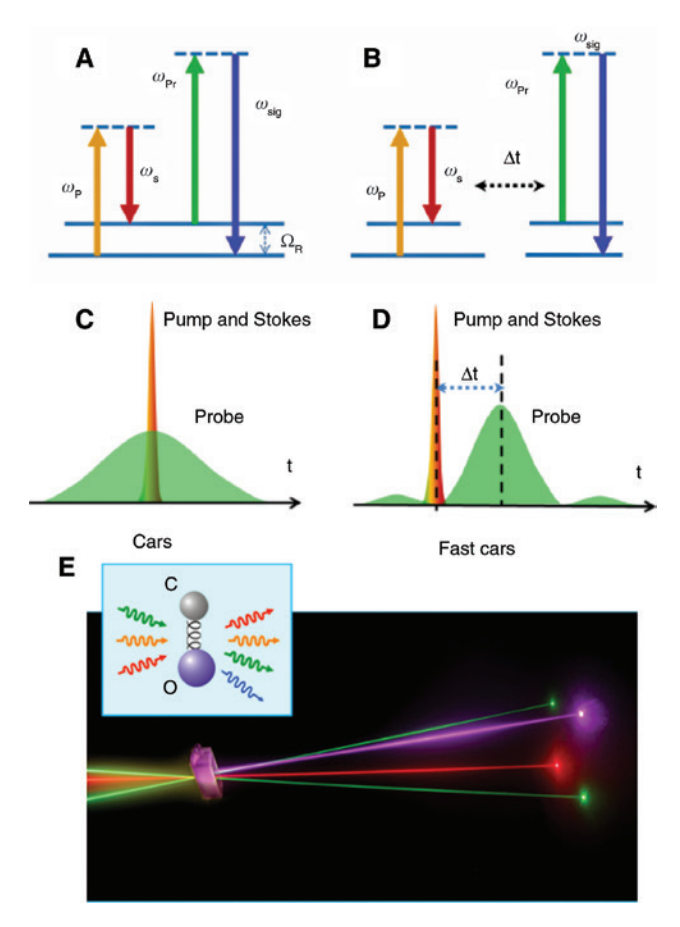


Figure 1: Comparison between the energy level diagrams and the laser configurations for the conventional CARS (A and C) and the time-resolved FAST CARS (B and D) spectroscopies. (E) Sketch of the laser beam configurations shows the pump (green), Stokes (red) and probe (green) laser beam incident on a sample generating the FAST CARS beam (blue). The inset shows a vibrating molecule emitting coherent signals. Adapted from Voronine et al. [1] and Shen et al. [11].

in Figure 1B and D [8, 9]. Here, the laser pulses 1 and 2 are applied to the sample first, and the optimally shaped laser pulse 3 is delayed. When laser 3 is applied to the sample and lasers 1 and 2 are not, the nonresonant processes do not occur. However, lasers 1 and 2 will have excited coherence between the vibrational levels in the molecule for which they are Raman resonant. If this coherence lasts longer than the delay, laser 3 will scatter from the coherence and still produce the FAST CARS signal at $\omega_{\rm sig}$. Spectral and temporal laser pulse shapes may be optimized to minimize the nonresonant background, for example, by placing lasers 1 and 2 (pump and Stokes) in the temporal node of the sinc-shaped pulse 3 (probe), and to enhance the resonant vibrational signal (Figure 1D).

Spontaneous Raman microscopy has been widely applied for the imaging of a variety of materials including

biological systems [12-15]. This has been a challenge due to the small Raman cross sections of biomolecules, leading to weak signals and long image acquisition time, in some cases taking multiple hours. Coherent Raman imaging provides a significant increase in imaging speed [6]. However, as the coherent Raman signal is proportional to N(N-1), where N is the number of molecules [7], the coherence enhancement decreases with the decrease of N and vanishes with N=1, that is, for the case of a single molecule. This makes it challenging to perform coherent Raman imaging at the nanoscale when the number of molecules N is small. Other Raman signal enhancement techniques, such as the plasmonic surface enhancement, may be combined with FAST CARS to further improve the sensitivity of nanoscale bio-imaging.

3 Quantum limits of surface enhancement

Nanoscale confinement of optical fields using plasmonic nanostructures provides an effective strategy for enhancing spectroscopic detection and imaging [16]. Localized surface plasmon resonances (SPRs) of metallic nanostructures and propagating surface plasmon polaritons (SPPs) may be used to obtain surfaceenhanced Raman scattering (SERS) signals [17–19]. The SERS effect is based on two mechanisms: electromagnetic mechanism (EM) and chemical mechanism (CM). The former is due to the local enhancement of the EM fields in the vicinity of the plasmonic nanostructures. The latter is due to the chemical interactions between the sample and the substrate, leading to the modification of the sample polarizability and the enhancement of the Raman scattering cross section. EM enhancement is usually the dominating effect in gold and silver nanostructures, leading to many orders of magnitude signal enhancement and sensitivity, which approaches the single-molecule limit [20-25].

There was much previous work on the applications of SERS to biosensing. However, less work was performed on the surface-enhanced nanoscale bio-imaging. There are several successful examples of proof-of-principle demonstrations of nanoscale bio-imaging using tip-enhanced Raman scattering (TERS) [26-33]. TERS is a combination of SERS and scanning probe microscopy, such as atomic force microscopy (AFM) and scanning tunneling microscopy (STM) [34–37]. AFM and STM performed with plasmonic probes made of gold and silver illuminated by laser radiation provide simultaneous topographic and

spectroscopic information with nanometer-scale spatial resolution. The Raman signal enhancement is based on the SERS EM and CM. The spatial resolution depends on the size of the probing tip apex, which may range from tens of nanometers down to a few atoms. A single hot spot generated at the tip apex provides both the Raman signal enhancement and the high spatial resolution. Large signal enhancement is crucial for achieving high imaging contrast and is strongly dependent on the tip design. Recent experiments demonstrated an extraordinarily high spatial resolution down to the sub-nanometer scale on carbon nanotubes (CNTs) [38] and porphyrin molecules in ultrahigh vacuum [39] and on DNA under ambient conditions [40]. TERS imaging was demonstrated on a variety of systems, but it is still a challenge for routine clinical bio-imaging. TERS imaging of a living biological cell has not yet been demonstrated. Such an experiment would require high-quality tips with strong signal enhancement for rapid non-destructive imaging and possible additional signal enhancement using other mechanisms such as resonance and/or coherence enhancements. The combination of the surface and the coherence enhancements is the focus of this review.

To better understand and make use of the SERS effect, we consider the limits of the surface enhancement, both EM and CM. Single plasmonic nanostructures such as silver and gold nanoparticles (NPs) can enhance the electromagnetic fields. However, the largest enhancement may be obtained by the coupling of multiple NPs [41-43]. Resonant optical dipole nanoantennas show strong near-field enhancement in the nanometer-size gap between NPs [44-48]. A similar behavior may be observed in TERS when the plasmonic tip is coupled to a metallic [49-52] or semiconductor [53] substrate. Figure 2A shows the schematics of the classical and quantum gap-mode TERS configurations. In the classical case, the gold tip induces an image dipole in the gold substrate, leading to the strong electric field enhancement and the corresponding Raman signal enhancement, which increases for the decreasing tip-sample distance. Classically, smaller gaps correspond to larger field enhancement. However, for the gaps smaller than ~1 nm, quantum tunneling (QT) of the electrons through the gap between the tip and the substrate leads to the decrease of the surface electron density of the tip and the corresponding decrease in the electric fields (Figure 2A, quantum regime). The quantum plasmonic effects were predicted [55–57] and experimentally demonstrated in systems of metallic NPs [58-62] and in TERS experiments using metallic tips and substrates [54, 63]. Figure 2B shows the tip-sample distance dependence of the gold photoluminescence signal

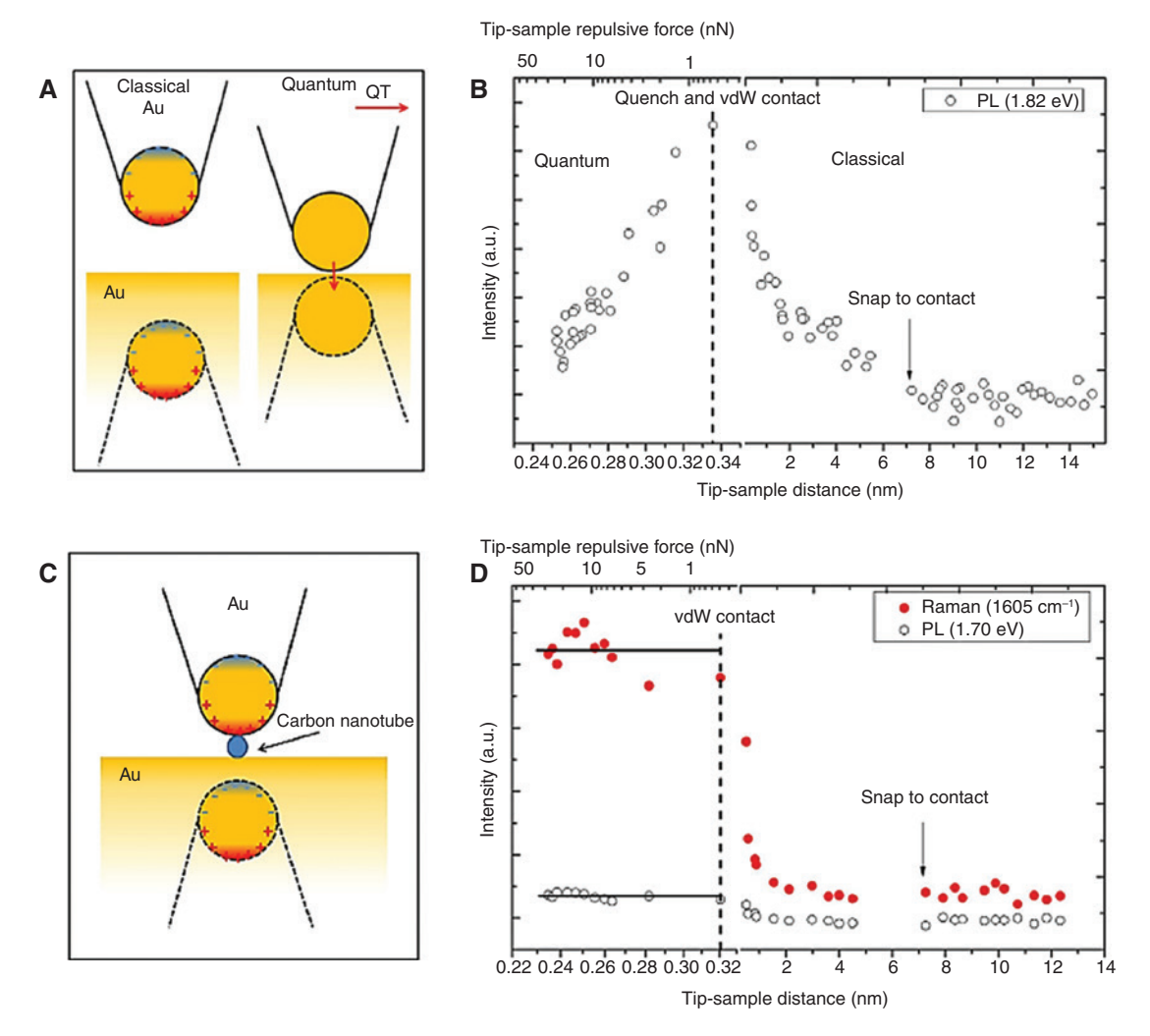


Figure 2: Quantum limits of surface enhancement revealed in (A) tip-enhanced photoluminescence (PL) of gold and (C) TERS signals of CNTs. Tip-sample distance dependence of the optical signals from the gold tip near the atomically flat gold substrate without (B) and with the CNT (D) junctions. PL and Raman signals are shown as open and red filled circles, respectively. Vertical dashed lines denoted by "Quench" and "vdW Contact" show the moments at which the signals begin to decrease and the tip-sample distance approaches the vdW diameter, respectively. Classical and quantum coupling schemes of the gold tip (A) and CNT (C) on gold substrates. Red arrow represents the QT current. Dashed lines show tip images in the substrates. Adapted from Zhang et al. [54].

before (classical regime) and after (quantum regime) the van der Waals (vdW) contact distance of ~0.33 nm. These two regimes correspond to the increase and decrease of the field enhancement with the decrease of the tip-sample distance, respectively. Figure 2C and D shows the schematic and tip-sample distance-dependent optical signals for the gap-mode TERS of a CNT, respectively. No significant quantum plasmonic quenching is observed after the vdW contact due to the larger Schottky barrier of the CNT which prevents electron tunneling. The unprecedented distance dependence control with sub-Angstrom resolution was obtained in these picometer-scale indentation experiments (Figure 2B and D). They give insights into the limits of the surface enhancement and may guide the

optimization of the nanoscale bio-imaging experiments. These results were made possible due to the recent progress in the scanning probe microscopy instrumentation with improved stability and distance dependence control of the combined state-of-the-art commercial systems (AIST-NT and Horiba).

Chemical enhancement effects have been observed in metallic systems but are usually weaker compared to the EM enhancement and are often masked. Recently, dramatic Raman signal enhancement was reported on ordered two-dimensional (2D) layered materials (graphene, MoS₂ and h-BN) [64–66]. The observations showed great promise to take advantage of the Raman scattering to identify chemical species using non-metallic

substrates. The enhancement on 2D layered semiconductor materials is dominated by the CM based on the change of the molecular polarizability caused by chemical interactions between the adsorbed molecules and the substrate. Various explanations of the CM were proposed, including (1) charge transfer resonances involving the transfer of electrons between the molecule and the conduction band of the substrate, and (2) molecular resonances [67-73]. Two-dimensional layered semiconductor materials provide excellent templates for studying the CM. CM enhancement may be increased by optimizing the electronic structure of the semiconducting substrates. These phenomena open the door to dramatically enhance Raman signals using both CM and EM effects.

Even when the quantum limit of the surface enhancement is reached, the optical signals may be further enhanced by using other mechanisms such as quantum coherence. Next, we consider the best-ofboth-worlds combinations of the surface and coherence enhancements using surface-enhanced coherent Raman spectroscopy.

4 Toward best-of-both-worlds surface-enhanced coherent Raman scattering

Quantum nano-biophotonics addresses the challenges of time-resolved nanoscale bio-imaging by taking advantage of various signal enhancement techniques such as CARS and SERS discussed above. In addition, high temporal resolution may be achieved using ultrashort laser pulses. The laser pulse shape may be optimized to suppress the nonresonant background and to control selectivity via the enhancement of the molecular signals. Various coherent nonlinear Raman techniques may be combined with surface enhancement to achieve an astonishing sensitivity [74]. For example, surface-enhanced femtosecond stimulated Raman scattering spectroscopy was developed using gold nanoantennas with embedded reporter molecules [75]. Various versions of surface- and tip-enhanced coherent anti-Stokes Raman scattering (SECARS and TECARS) techniques were demonstrated on ensembles down to a few and even single-molecule sensitivity. Several recent review papers described these developments [44, 74, 76–80]. Here, we focus on the SECARS techniques in which the physics of the interplay between the coherence and the surface enhancement is, in our opinion, most clear.

4.1 SECARS

The first experimental demonstrations [81, 82] and theoretical analysis [83] of SECARS were followed by several attempts to simulate [84, 85] and improve the signal enhancement [86–89], optimize substrates [85, 90-93], add temporal resolution [94, 95], suppress the nonresonant background [85, 94, 96], achieve singlemolecule sensitivity [95, 97, 98] and perform microscopic [99, 100] and nanoscale bio-imaging [101–104]. These studies revealed and addressed the controversies such as the lower experimental enhancement factors (EFs) than those expected in theory, the comparison between SERS and SECARS, the limited reproducibility, the challenges of single-molecule detection and biological applications. The latter have been one of the main motivations for the development of SECARS. Here, we review these challenges and speculate on future perspective solutions.

Large surface EFs are expected in SERS and SECARS. The EM enhancement via SPR field enhancement and CM enhancement via charge transfer both contribute to the EFs as discussed above, with the larger effect of the EM on noble metal substrates. The EFs for SERS are defined with respect to the spontaneous Raman scattering (SpRS). However, the SECARS EFs can be defined with respect to (i) conventional CARS without the surface enhancement by plasmonic nanostructures (EF_{SECARS/CARS}), or with respect to (ii) SERS without the coherence enhancement $(EF_{SECARS/SERS})$ or with respect to (iii) SpRS without both surface and coherence enhancements (EF_{SECARS/SpRS}). The latter is the total SECARS EF, which has all the contributions of the various enhancement mechanisms. These EFs are summarized in Table 1, where the column labels indicate the techniques whose EFs are considered with respect to the corresponding techniques with the row labels. The theoretically expected EF values are shown in bold, and the corresponding experimentally obtained EF values are given in parentheses together with the plasmonic substrates, type of SECARS and references. Femtosecond SECARS is based on the femtosecond laser pulses, while the FAST SECARS is based on the combination of femtosecond and shaped picosecond laser pulses. These techniques and experimental demonstrations are discussed in more detail below.

The coherence enhancement of CARS with respect to the SpRS may reach ~106 and depends on the squared number of molecules [7]. The surface enhancement may reach many orders of magnitude due to the nonlinear dependence of SECARS on the local electric fields (Figure 3) [91]. The EM enhancement leads to EFs which

Table 1: EFs of various spectroscopic techniques with the surface and/or coherence enhancement (column labels) with respect to the techniques without these enhancements (row labels) based on the theoretical expectations (bold) and experimentally observed (in parentheses).

	CARS	SERS	SECARS
SpRS	10 ⁶ (10 ⁶ , various	10 ⁴ – 10 ¹² (10 ¹⁰ , various	10 ¹⁴ -10 ³⁰ (10 ¹¹ , plasmonic
	samples [7])	samples [105])	quadrumer, fsec SECARS [98])
CARS	_	-	108-1024
			(10, colloidal NPs, fsec SECARS [87]; 10 ⁵ , deterministic, fsec
			SECARS [91]; 10 ⁷ , random aggregated NPs, FAST SECARS [94])
SERS	-	-	10 ¹⁰ -10 ¹⁸ (10 ³ , deterministic, fsec SECARS [91])

fsec. Femtosecond.

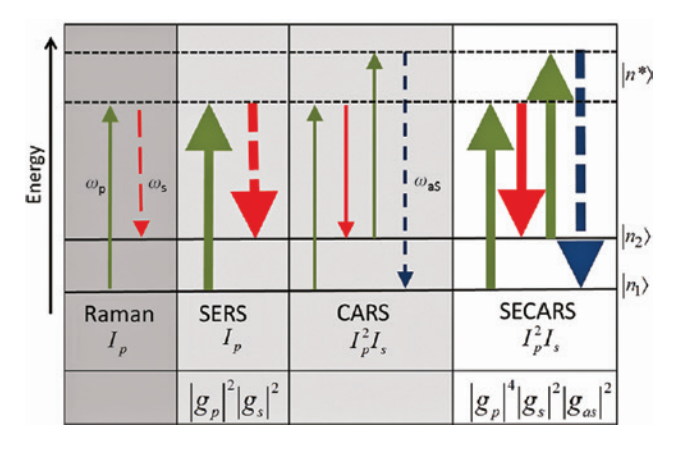


Figure 3: Surface and coherence enhancement of Raman signals. Schematic band energy diagram showing transitions in different Raman processes and their dependence on the pump (I_p) and Stokes (I_s) intensities and the corresponding local electric field enhancement (g). Adapted from Steuwe et al. [91].

are proportional to the near-field EFs (g) in hot spots of plasmonic nanostructures, which can reach values $g \sim 10^1 - 10^3$ depending on the geometry and composition. The corresponding $\mathrm{EF}_{\mathrm{SERS}} \approx |g_{\mathrm{p}}|^2 |g_{\mathrm{s}}|^2$ can reach values of $10^4 - 10^{12}$, where g_{p} and g_{s} are the pump and Stokes near-field EFs, respectively. Such large EFs were experimentally observed [105]. However, the SECARS EFs have both surface and coherence contributions of $\mathrm{EF}_{\mathrm{SECARS/CARS}} \approx |g_{\mathrm{p}}|^4 |g_{\mathrm{s}}|^2 |g_{\mathrm{as}}|^2$ and $\mathrm{EF}_{\mathrm{SECARS/SERS}}$, which can theoretically reach $\sim 10^8 - 10^{24}$ and $\sim 10^{10} - 10^{18}$, respectively. Here, g_{as} is the anti-Stokes signal near-field EF. Therefore,

the total SECARS EF over spontaneous Raman, denoted $\rm EF_{SECARS/SpRS}$, can reach $\sim 10^{14} - 10^{30}$, which has not yet been experimentally demonstrated. Recent progress in instrumentation and nanofabrication has been pushing these EFs up toward theoretical predictions. Further improvements are expected from a better understanding of the experimental challenges, inhomogeneous sample properties, effects of laser pulse shaping and chemical interactions. Some of these are addressed in more detail below.

As one of the SECARS schemes, surface-enhanced FAST CARS is developed to suppress the unwanted nonresonant background. Therefore, there is a competition of two effects which determines the signal-to-noise ratio of the surface-enhanced FAST CARS signals, namely, the signal enhancement and the nonresonant background suppression. The background suppression may be achieved by the temporal delay of the pump/Stokes and probe laser pulses. However, this often decreases the overall signal due to the temporal decay of the coherence. In practice, an optimal time delay is used to obtain the maximum signal with the minimum background. On the other hand, there are also techniques in which the enhancement may be optimized at the zero time delay with the presence of the nonresonant background. For example, heterodyne CARS techniques used in broadband CARS microscopy [106-110] may be combined with SERS and TERS to improve signal enhancement. In heterodyne CARS, the weak molecular resonant signals may be enhanced by coherently mixing with the nonresonant background. Previously, we succeeded in eliminating the FWM background in surface-enhanced FAST CARS [9, 10, 94]. However, by properly introducing some background and controlling the phase, it may be possible to improve the detection sensitivity. The interference between the coherent resonant signal and the coherent nonresonant background may be controlled by phase and amplitude pulse shaping. For example, this control may be achieved by making fine adjustments to the probe field shape [111]. Spectral asymmetry of the probe may produce a stronger temporal probe field at the node and the correspondingly stronger FWM background which provides flexibility of controlling both the phase and intensity of the heterodyne signals. Near-field pulse shaping needs to be carefully designed to optimize the EFs in surface-enhanced broadband heterodyne CARS.

Another factor which needs to be carefully considered is the saturation of the coherent Raman transitions in analogy to the corresponding saturation of the Raman gain in stimulated Raman scattering [112, 113]. Here, because of the strong field enhancement, the Raman signal may get saturated before reaching the predicted

30 orders of magnitude enhancement. This effect will be stronger in molecular systems with large Raman scattering cross sections.

4.2 SECARS on colloidal NPs

A single plasmonic sphere is the simplest model system for SECARS. Theoretical analysis estimated the EF value of 10¹² for a monolayer of benzene on a silver particle [83]. However, the experimental demonstration of this configuration is not trivial. A simpler experimental approach is an ensemble of the colloidal plasmonic spheres dispersed in a neat liquid of interest. It was also considered in the first theoretical SECARS analysis and compared with the single sphere model [83]. Lower experimentally observable EFs were predicted based on the averaging over the ensemble of spheres and competition with the background bulk CARS signal. The NP concentration dependence was used to estimate the minimal concentration needed to detect the SECARS signal and was found to be $\sim 10^{-5}$ g/cm³. The sphere ensemble approach is particularly significant for the investigation of biological systems with preferable minimized sample perturbation. However, the challenges mentioned need to be carefully considered in the design of biological applications. Another challenge is the potential sample degradation due to the high power of ultrashort laser pulses. One important difference between the typical SERS and SECARS experiments is that the former is usually performed using continuos wave lasers, while the latter is performed using ultrashort laser pulses. Therefore, special attention has to be paid to the heat generation in the SECARS experiments and the heat resistance of the investigated sample system. Two pioneering experimental works investigated SECARS on colloidal solutions using nanosecond [82] and femtosecond laser pulses [87].

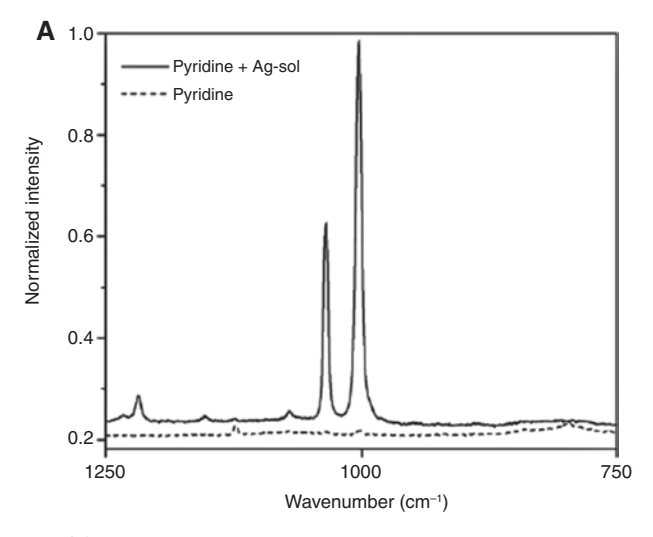
Nanosecond SECARS experiments on benzene, chlorobenzene and toluene were performed in colloidal solutions of silver NPs and revealed up to ~102 EFs and an improvement in signal-to-noise ratio [82]. The SECARS signals were collected at right angles with respect to the pump and Stokes beams, which were incident on a sample at a small angle (1°-3°). The pump wavelength dependence showed the maximum signal enhancement at ~500 nm, which was red shifted with respect to the SPR of the silver colloid. This first demonstration of the SECARS in a colloid solution did not perform a careful sample characterization or make a quantitative comparison with the previous theoretical predictions. The authors noted a narrower pump excitation wavelength profile than what was expected from the width of the SPR. They explained

it by the more restricting resonance conditions of the four photons involved in the CARS process. For example, the red-shifted detuning of the pump wavelength away from the SPR requires even further detuning of the Stokes wavelength, which leads to a fast decrease of the SECARS signal. This indicated the need for improving the design of plasmonic nanostructures to optimize the SPR frequency and width.

Femtosecond SECARS experiments in silver colloids were performed on pyridine and showed only a factor of 10 EFs for the pump wavelength of 550 nm for the SECARS collected in the forward direction and no enhancement for other pump wavelengths [87]. Another difference from the nanosecond SECARS was the absence of the signal enhancement collected at right angles. Interestingly, the observed SERS EFs of ~104 from the same silver colloid were three orders of magnitude larger than the corresponding SECARS EFs. The comparison of the SERS and spontaneous Raman spectra of pyridine in the silver colloid is shown in Figure 4A. In contrast, smaller enhancement is shown for the SECARS signals with different concentrations of silver colloid in Figure 4B. Note that the spectra in Figure 4A and B have mismatched x axes. The two strongest vibrational transitions of pyridine around 1000 cm⁻¹ are clearly seen in the SERS spectra but are less resolved in the SECARS spectra due to the lower spectral resolution from the broadband femtosecond laser pulses. Also, the surface-enhanced nonresonant FWM background may contribute to the observed SECARS spectra [114-117]. The concentration dependence showed the maximum SECARS enhancement for 10% concentration of the silver colloid. The enhancement decreased for the larger concentration, probably due to the scattering of the lasers and signal away from the phased-matched forward direction by the silver NPs. These experiments indicated the dependence of the SECARS signals on several parameters such as the properties of the silver colloids, concentration, laser wavelength, intensity and phase matching. Optimization of these conditions is challenging and might be more easily achieved in other SECARS configurations such as in random aggregates of NPs or in deterministically designed nanostructures. These are discussed next.

4.3 SECARS on random nanostructures with local phase variations

The problem of small EFs in femtosecond SECARS on colloids was addressed by optimizing the random gold NP self-assembly deposited on glass substrates [90]. SECARS of oxazine 720 was measured as a function of the number



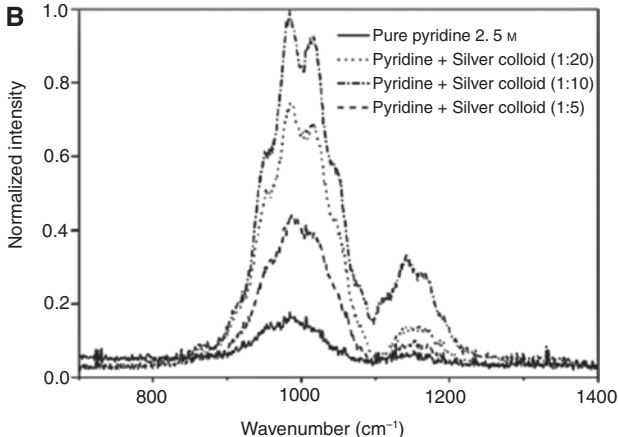


Figure 4: SECARS on colloidal NPs.

(A) Raman spectra of pyridine recorded without (dashed, spontaneous Raman) and with (solid, SERS) the addition of silver colloid. (B) Femtosecond SECARS spectra of pyridine for different concentrations of silver colloids (dashed curves) compared with the conventional CARS spectrum of pyridine alone (solid curve). Note that the spectra in (A) and (B) have mismatched *x* axes. Adapted from Namboodiri et al. [87].

of gold NP depositions, and the maximum $\rm EF_{\rm SECARS/CARS}$ of 10 was obtained for 11 depositions from the 1600 cm⁻¹ signal. One of the reasons for such small EFs can be the spatial averaging over a large surface area, which includes locations with and without so-called "hot spots," that is, locations with large EFs due to small inter-particle gaps and SPR matching the incident laser wavelength and CARS signals. The EF was optimized by increasing the number of NP depositions, leading to a larger number of hot spots and to the optimal match of the SPR. However, small EFs and large spatial variations from area to area were observed even in the optimized substrates. Other possible reasons could be the nonresonant background contributions and local phase variations as discussed next.

Many parameters play a role and may be optimized in femtosecond SECARS experiments. Nano-optical biosensing and imaging require large signal enhancement, small background, short detection time and high spatial and spectral resolution. Ultrashort laser pulses provide unique opportunities to detect nonlinear optical signals and to study ultrafast time-resolved dynamics. They also provide a range of control parameters such as the wavelengths, polarizations, spectral and temporal amplitudes and phases to optimize the nonlinear signals. Recently, we developed a surface-enhanced FAST CARS technique which is a type of the time-resolved SECARS (tr-SECARS) where the pump and Stokes pulses are temporally delayed with respect to the shaped probe pulse (Figure 5A) [94]. The probe pulse was shaped as a sinc function using a home-built pulse shaper in order to place the pump and Stokes pulses in the temporal node of the probe to suppress their temporal overlap and the nonresonant FWM background. A similar FAST CARS setup was previously used to detect Raman signals from bacterial endospores [9, 10]. Our surface-enhanced FAST CARS technique (also abbreviated as FAST SECARS) increased the conventional

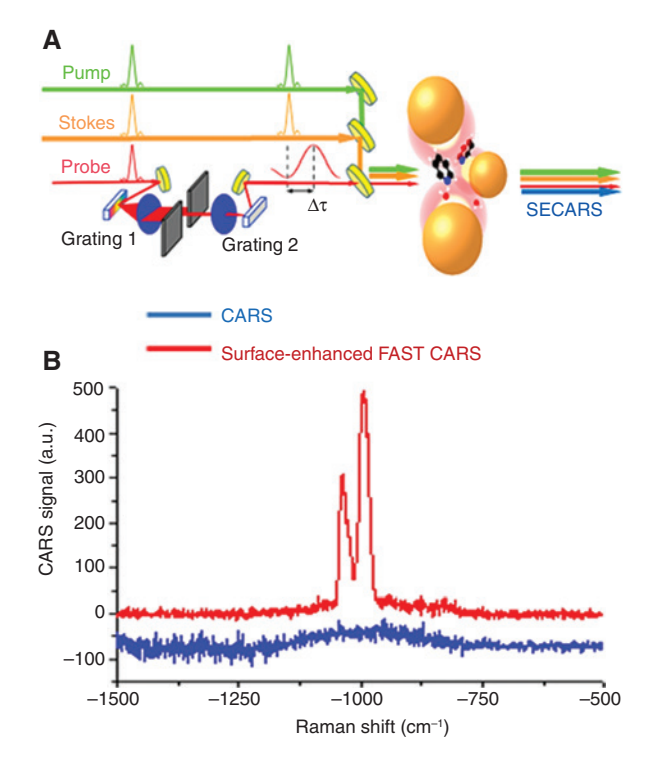


Figure 5: Surface-enhanced FAST CARS on random nanostructures. (A) Experimental scheme of the surface-enhanced FAST CARS spectroscopy. (B) Surface-enhanced FAST CARS (red) reveals traces of hydrated pyridine molecules on the surface of gold NP aggregates with higher sensitivity than the conventional CARS (blue). Adapted from Voronine et al. [94].

CARS signal intensity by $EF_{SECARS/CARS}$ of ~10⁷ and was used to detect trace amounts of water on the surface of random aggregated gold NPs (Figure 5B). A spectral resolution of ~3 cm⁻¹ was achieved by narrowing the bandwidth of the probe pulse using the slit of the pulse shaper. This facilitated the observation of the 7 cm⁻¹ spectral shift of the position of the pyridine ring breathing mode due to the interaction with water. The FAST SECARS temporal signal provided direct observations of the dephasing dynamics of the pure bulk pyridine and the surface-bound water-pyridine complexes. The latter exhibited shorter dephasing times compared to the bulk pyridine. This timeresolved configuration of the SECARS provides a possibility to study biological systems simultaneously with a high

spatial and temporal resolution. The aggregated colloidal gold NPs showed large SECARS EFs which, however, still represented average quantities over micrometer-scale observation areas and were smaller than expected. We performed additional investigations by analyzing the spatial dependence of the SECARS EFs and local phases.

We also measured the spatial variation of the shape of the FAST SECARS spectra of pyridazine on randomly aggregated gold NPs and obtained insights into the nature of low SECARS EFs [85]. Figure 6A shows a schematic SECARS process where three ultrashort laser beams (pump, Stokes and probe) excite the sample of aggregated gold NPs on a glass substrate and generate locations of enhanced local fields (hot spots) with different phases

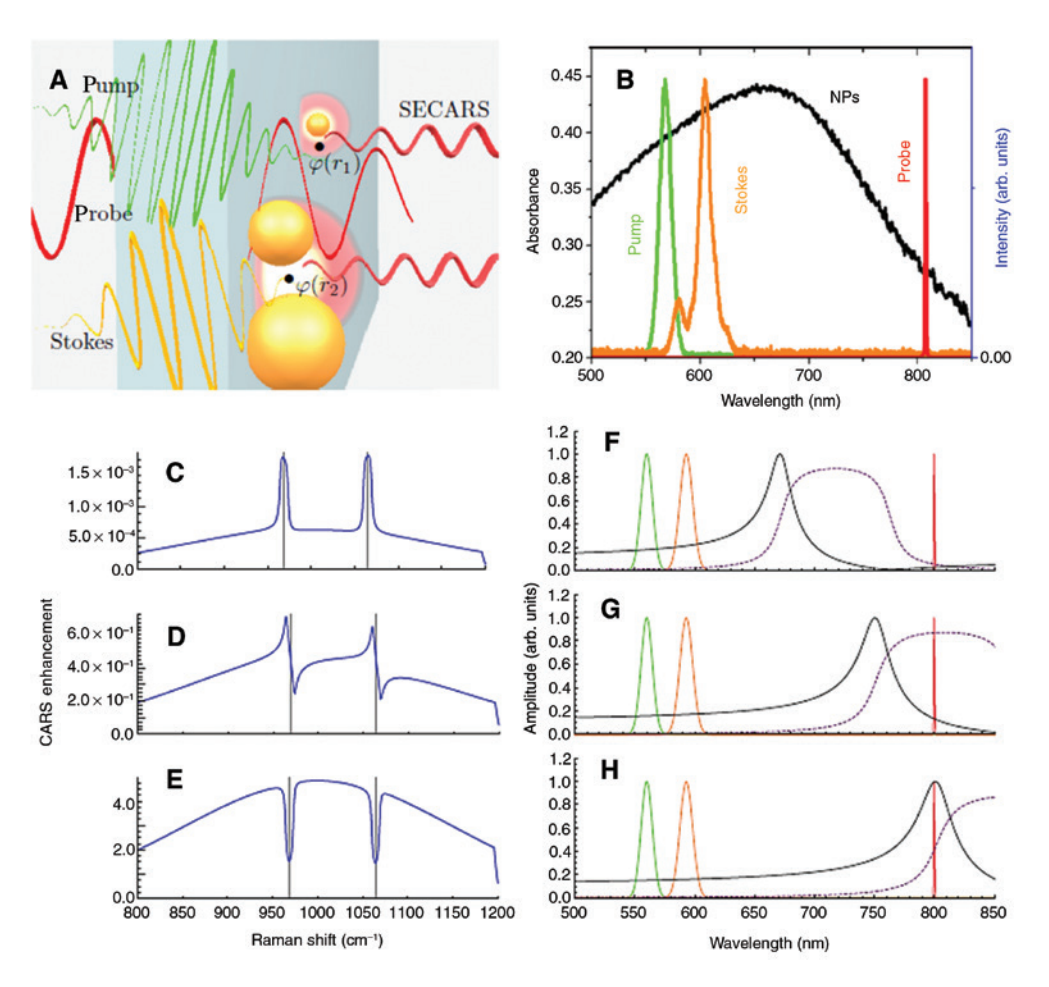


Figure 6: Nature of SECARS.

(A) Schematic picture of the SECARS process: three ultrashort laser pulses (pump, Stokes and probe) are focused on the sample of randomly aggregated gold NPs on the surface of glass inducing SECARS signals from pyridazine molecules in different spatial locations with different local phases $\phi(r)$ which lead to different spectral shapes and low average EFs. (B) Average absorbance spectrum of the aggregated gold NPs (black, NPs) overlapping with the laser pulse spectra used in the SECARS experiments. (C-E) SECARS spectra of pyridazine simulated with SPR wavelengths at 672, 751 and 802 nm, respectively. (F-H) The corresponding electric field amplitudes of the incident pump (green), Stokes (orange) and probe (red) laser pulses with normalized amplitudes (solid black) and phases (purple dashed) of the local field enhancement. For certain ratios of the field amplitudes and certain local phases, it is possible to obtain almost complete destructive interference between the incident and enhanced local fields leading to the formation of "cold spots" with negative EFs. Adapted from Hua et al. [85].

 $\varphi(\mathbf{r}_i)$. Averaged SECARS signals obtained from a fewmicrometer-size area contain many hot spots with different local phases leading to different SECARS line shapes (e.g. peaks, dips and dispersive line shapes) which may destructively interfere, leading to low average EFs. Figure 6B shows the average absorbance spectrum of the aggregated gold NPs (black, NPs) overlapping with the laser pulse spectra used in the SECARS experiments. The broad absorbance spectrum consists of an average of many SPR spectra with different frequencies and spectral phases which modify the phases of the resulting SECARS signals (Figure 6F-H) and the SECARS spectral line shapes (Figure 6C-E). For certain ratios of the nonresonant background and number of surface pyridazine complexes and for certain SPR positions with respect to the laser beams, it is possible to obtain almost complete destructive interference between the incident and enhanced local fields, leading to the formation of "cold spots" with negative EFs (Figure 6C and F). Better design of the plasmonic nanostructure substrates and better control of the laser excitation are needed to maximize the SECARS EF via constructive interference.

We also observed more complex line shapes in the SECARS of pyridazine on aggregated gold NPs than were expected based on the simulations described above [96]. In addition to the peaks, dips and dispersive line shapes, we observed a peculiar "peak-dip" line shape which consisted of both a peak and a dip at two closely spaced pyridazine transitions. This line shape may be explained as resulting from the interference of signals from two different molecular complexes, one of which is present in bulk and the other is near the plasmonic surface. The peak-dip effect may be present if these complexes have different relative ratios of the intensities of the Raman signals from different transitions. The complex SECARS line shapes are sensitive to the minor differences in the intensity ratios and may be used as sensitive probes of molecular environment. The SECARS EFs may be improved by optimizing the nanostructured substrate design, by the control of local phases by laser pulse shaping and by the optimization of the sample conditions, such as the contributions of solvent, and various molecular complexes. Next, we discuss these approaches.

4.4 SECARS on deterministic nanostructures

The SECARS substrates may be optimized by focusing either on a single plasmonic nanostructure or on a periodic nanostructure array. Previous work on single plasmonic nanostructures showed first SECARS demonstrations of adenine on isolated gold NPs with EF $_{\mbox{\scriptsize SECARS/CARS}}$ of $\sim\!10^3$ [86], followed by tip-enhanced implementations of SECARS on DNA, CNTs and subcellular organelles using plasmonic tips [80, 88, 101, 103, 104] with $EF_{SECARS/CARS}$ between ~10 and 106, and approached single-molecule sensitivity using plasmonic NP dimers [89, 95] and quadrumers [98] with $EF_{\text{SECARS/SpRS}}$ of ${\sim}10^{11}\text{,}$ approaching the theoretical limits.

The second approach to optimize the SECARS substrates is via the design of periodic arrays of plasmonic nanostructures. Cross-dipole nanoantennas were previously arranged in a 2D array pattern providing the optical near-field enhancement of ~128 in the hot spots at the centers of the cross-antennas (Figure 7) [92]. We theoretically estimated $\text{EF}_{\text{SECARS/CARS}}$ between ${\sim}10^{11}$ and 10^{12} for typical values of SPR line widths [85]. Similar substrates made of crisscross dimer arrays were theoretically investigated and showed large field enhancements and same spatial hot spot regions for the three incident fields with $EF_{\text{SECARS/CARS}}$ of ${\sim}10^{16}$ [118]. The cross nanoantennas provide opportunities to engineer the near-field polarization profile [119] and to optimize the cross-polarized SECARS signals. Nanoantenna array metasurfaces [120] may be

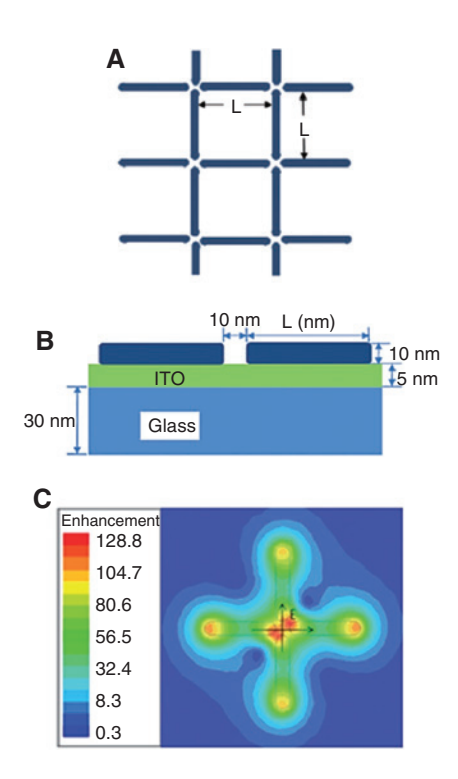


Figure 7: Plasmonic metasurface for SECARS. (A) Cross-dipole metasurface with dipole arms arranged in an array pattern. (B) The array elements are gold strips on an indium tin oxide (ITO)/glass layer illuminated from the top by a 1000-nm plane wave. (C) Near-field enhancement map in a plane 15 nm above the ITO surface shows two orders of magnitude enhancement of the electric

field in the dipole gap. Adapted from Nevels et al. [92].

designed to optimize the amplitude and phase properties of the SECARS substrates.

The first experimental demonstration of the SECARS on periodic plasmonic substrates was performed on fabricated nanovoid surfaces and commercial (Klarite) substrates with $EF_{SECARS/CARS}$ of ~105 and $EF_{SECARS/SERS}$ of ~103 (Figure 8) [91]. Femtosecond laser pulses were focused to ~1-um spots on the nanovoid surfaces with variable nanovoid thickness and diameters between 400 and 1000 nm, and on the Klarite surface consisting of micrometer-size pyramidal pits. The substrate structural parameters were varied to optimize the SECARS signals by matching the SPR frequencies to the incident lasers. The plasmon-aided mechanism was proposed (Figure 8A), in which the incident photons are coupled to plasmons which generate coherent anti-Stokes-shifted plasmons that are coupled into the outgoing SECARS photons. Despite the low spectral resolution of ~50 cm⁻¹ due to the broadband excitation and contributions of the surface-enhanced FWM background, the authors were able to prove the molecular selectivity by distinguishing the SECARS spectra of several molecules (Figure 8B and C). They detected submonolayer concentrations of cyanide and achieved close to singlemolecule sensitivity. The advantage of the nanovoid

substrates was their broadband SPR range, which can match the incident laser and signal wavelengths in the same spatial location. The design of such substrates may be further optimized for the purpose of achieving optimal SECARS EFs.

4.5 Surface-enhanced CARS of single and/or few molecules

tr-SECARS microscopy was for the first time demonstrated on trans-1,2-bis-(4-pyridil) ethylene (BPE) molecules attached to single gold plasmonic dimers encapsulated in porous silica shells (Figure 9) [95]. The observed SECARS spectra were attributed to the ensembles of a few and even single molecules in the gaps between the plasmonic nanoantenna junctions. The evidence for single-molecule sensitivity was obtained by analyzing the temporal traces of the vibrational beating signals excited on and off resonance with the BPE vibrational transitions using timedelayed pump/Stokes and probe pulses (Figure 9). The observed vibrational quantum beats of the ensemble bulk signals decayed after ~1 ps. However, some of the single nanostructure signals persisted for the 10-ps duration of

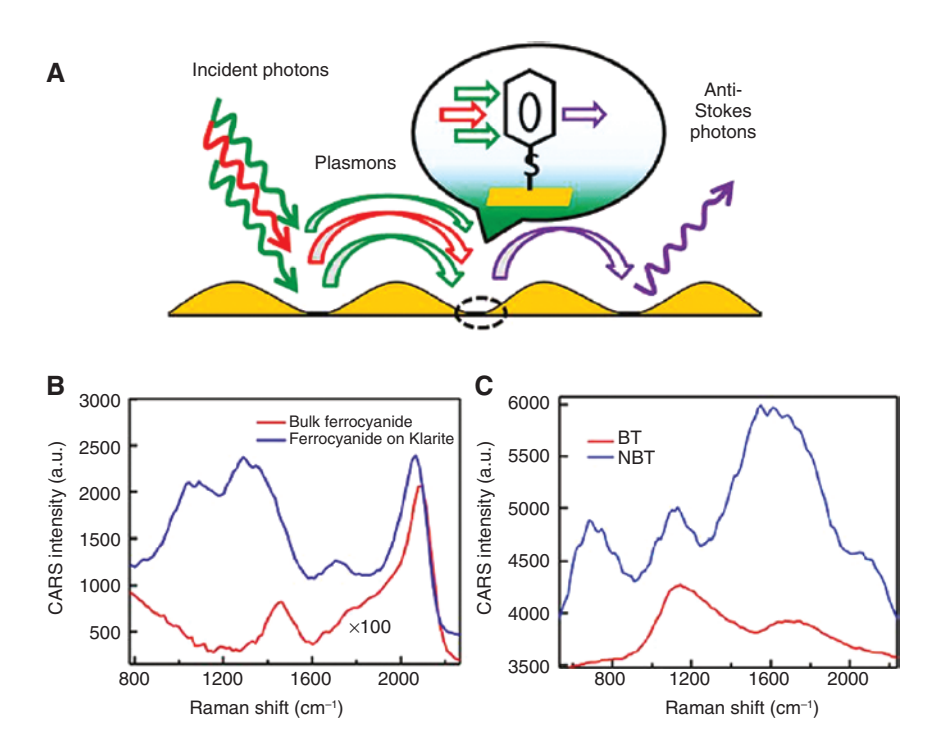


Figure 8: SECARS on a deterministic substrate.

(A) Schematic of plasmon-aided SECARS on a deterministic substrate: incoming pump and Stokes radiation couples into surface plasmons that interact coherently with molecules on the surface and scatter into the outgoing CARS photons. (B) SECARS spectrum (blue) of submonolayer ferrocyanide on a plasmonic substrate (Klarite) compared with the CARS spectrum (red) of the same bulk ferrocyanide. (C) SECARS spectra of nitrilobenzenethiol (NBT) and benzenethiol (BT) on Klarite. Adapted from Steuwe et al. [91].

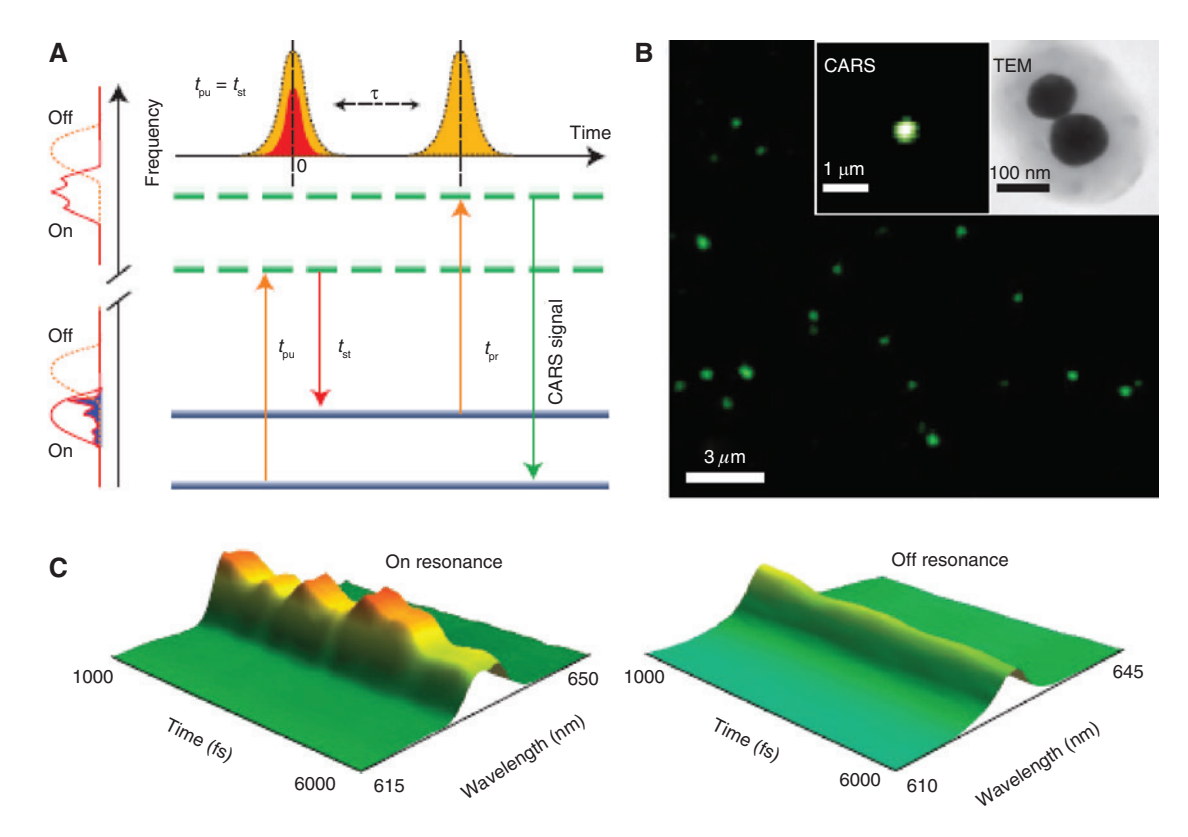


Figure 9: tr-SECARS microscopy of BPE molecules on single plasmonic dimers.

(A) The energy diagram shows the SECARS excitation scheme with the time delay τ between the pump/Stokes pair and the probe pulse.

(B) CARS image of isolated plasmonic dimers. Inset: CARS image of a single dimer and the corresponding transmission electron microscopy image. (C) Spectrally and temporally resolved CARS signals of a single dimer acquired on (left) and off (right) resonance. Quantum beats corresponding to the molecular SECARS signals disappear in the off-resonance signals. Adapted from Yampolsky et al. [95].

the experiment. This was attributed to the absence of the dephasing and, therefore, the single-molecule origin of the SECARS signals.

Another evidence for single-molecule SECARS sensitivity was obtained from para-mercaptoaniline (p-MA) and adenine molecules on single plasmonic gold quadrumer nanostructures with plasmonic Fano resonances [98]. Single-molecule sensitivity with the estimated $\mathrm{EF}_{\mathtt{SECARS/SDRS}}$ of ~1011 was demonstrated on these molecules with small Raman cross sections. The linear scattering spectrum of the plasmonic substrate nanostructure was optimized to match the excitation and signal fields in order to suppress absorption of the pump field and to enhance scattering of the anti-Stokes signal by the subradiant and superradiant modes, respectively (Figure 10A and B). The quadrumer consisted of four coupled gold nanodisks whose diameters and gap sizes may be used as the control parameters to match the SPR and excitation/signal frequencies. The spatial overlaps between the field distributions need to be optimized so that the excitation hot spots from the pump, Stokes and probe lasers are in the same spatial

locations. Figure 10C and D shows spatial field enhancement intensity distributions and SECARS enhancement maps, respectively, indicating good localization in the center of the quadrumer and overlap. The evidence for signal molecule sensitivity was provided by the bi-analyte statistical analysis.

Next, we discuss the coherence effects in these single-molecule SECARS experiments. According to our previous theoretical analysis, the coherence enhancement effect may be expressed as the ratio of the number of photons generated through the CARS, $\langle n_4^{\rm coh} \rangle$, to the number of incoherent spontaneously scattered Raman photons, $\langle n_4^{\rm incoh} \rangle$, as

$$\frac{\left\langle n_{4}^{\text{coh}} \right\rangle}{\left\langle n_{4}^{\text{incoh}} \right\rangle} \cong \lambda^{2} \frac{N(N-1)}{NV} \frac{\left| \rho_{\text{bc}} \right|^{2}}{\rho_{\text{cc}}} R, \tag{1}$$

where λ is the wavelength, V is the sample volume, R is the sample radius, ρ_{cc} is the population of the ground state c, ρ_{bc} is the coherence between vibrational levels b and c and N is the number of molecules [7]. Eq. (1)

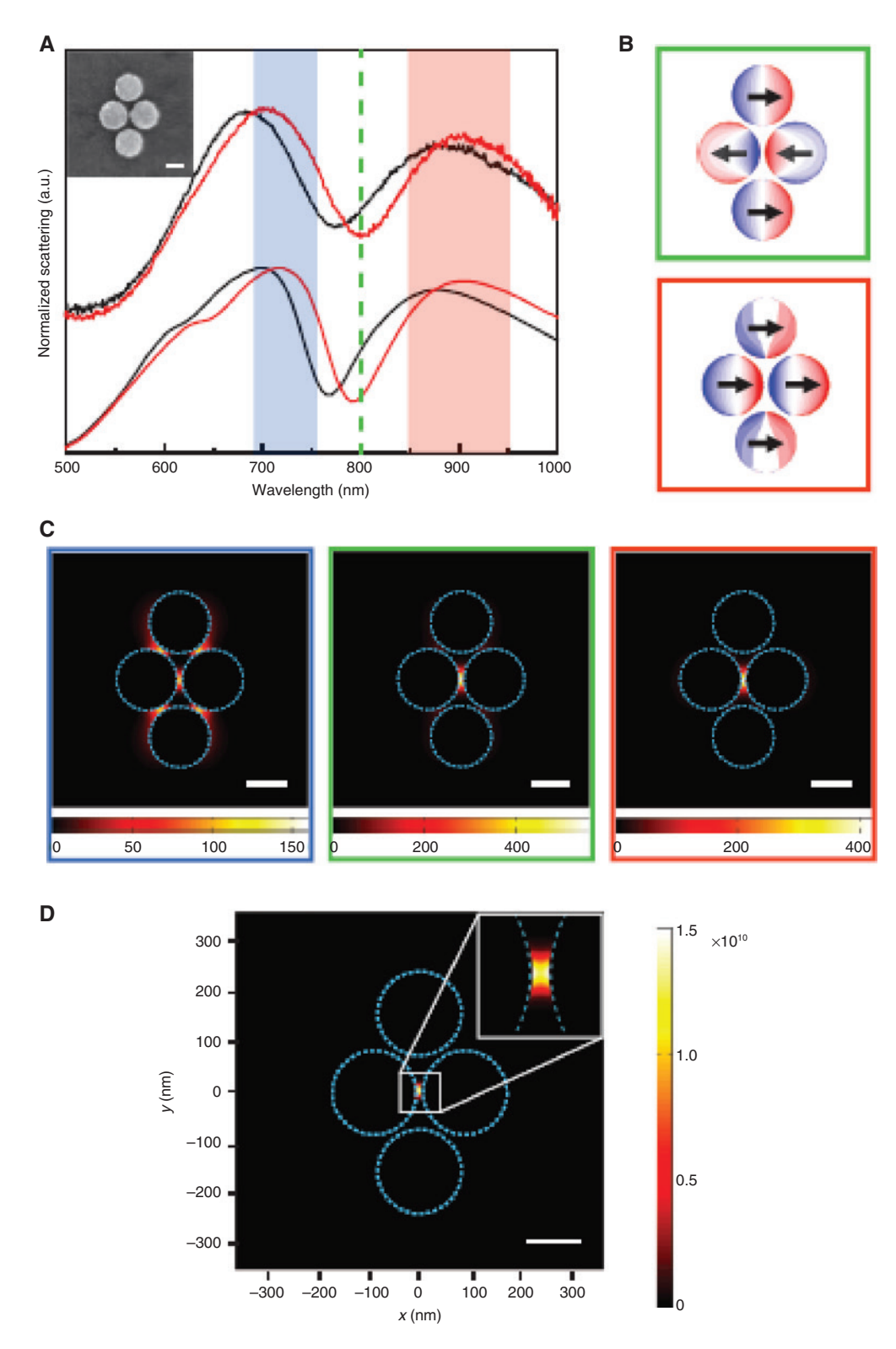


Figure 10: SECARS on a single gold quadrumer nanostructure using a plasmonic Fano resonance. (A) Experimental (top) and calculated (bottom) linear scattering spectra of a single quadrumer without (black) and with (red) p-MA molecules. Green dashed line indicates the pump beam at 800 nm; red and blue zones show the Stokes and anti-Stokes scattering regions. The inset shows a scanning electron microscopy image of the quadrumer. (B) Charge densities on the top surface of the quadrumer excited at 800-nm pump (top) and 900-nm Stokes (bottom), corresponding to the subradiant and superradiant modes, respectively. (c) Field enhancement intensity distributions at the anti-Stokes (left), pump (middle) and Stokes (right) frequencies, and (D) the corresponding SECARS enhancement map. Scale bar, 100 nm. Adapted from Zhang et al. [98].

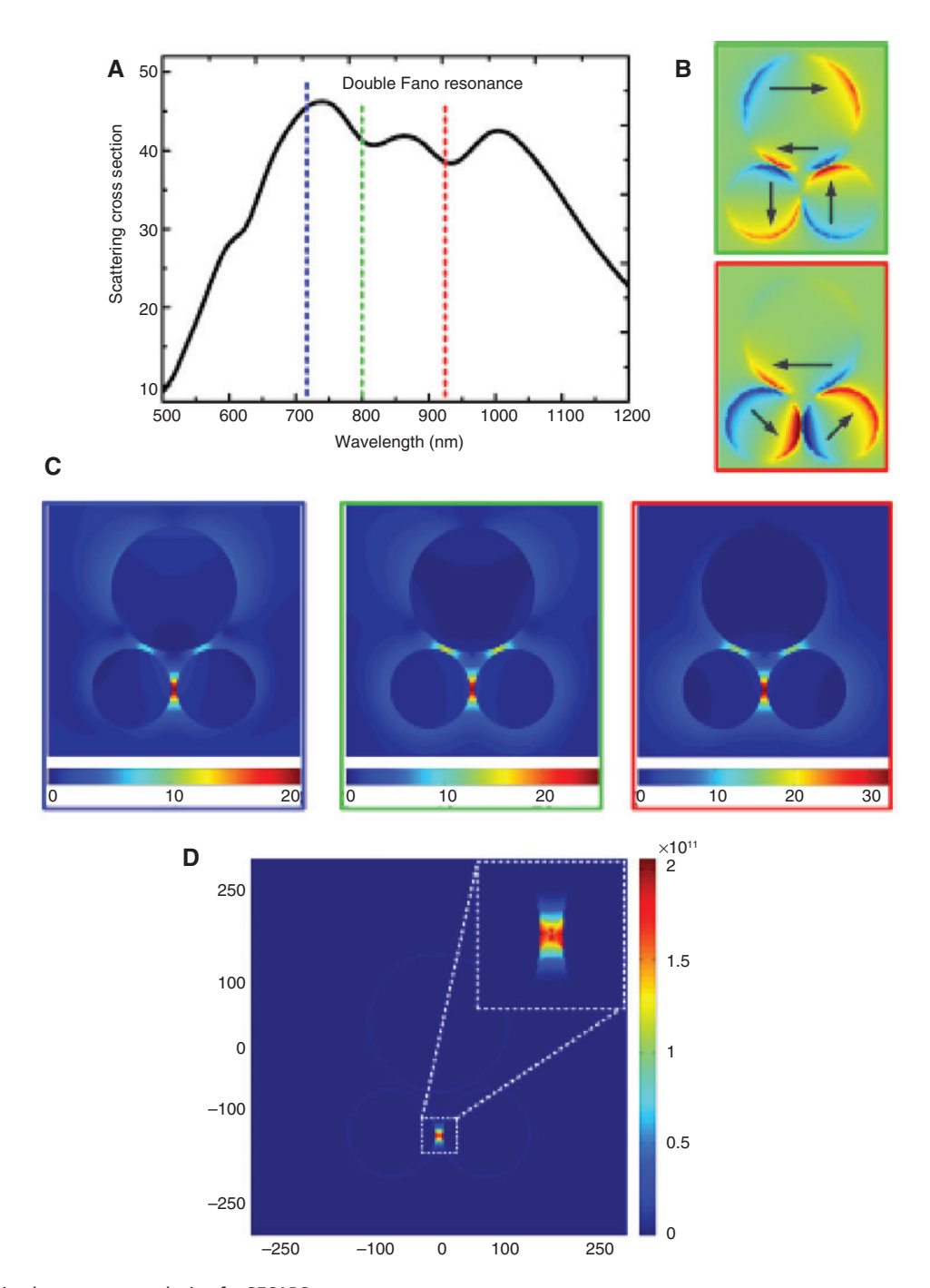


Figure 11: Optimal nanostructure design for SECARS.

(A) Scattering spectrum of the plasmonic gold disk trimer nanostructure. Blue, green and red dashed lines correspond to the anti-Stokes (710 nm), pump (800 nm) and Stokes (916 nm) fields. Two dips of the double Fano resonance are matched with the pump and Stokes fields to minimize absorption losses. (B) Spatial electric field distributions corresponding to the Fano resonance dips in (A) show two subradiant modes with out-of-phase oscillating electrons in the disks shown by arrows. (C) Near-field enhancement distributions in a plane 1 nm above the top surface of the trimer at the anti-Stokes (left), pump (middle) and Stokes (right) frequencies with the corresponding SECARS map in (D). Adapted

shows that in the single-molecule limit of N=1, the N^2 -type molecular coherence enhancement vanishes and the quantum coherence $\rho_{\rm bc}$ cannot be used to enhance the Raman signal. Intuitively, Eq. (1) shows that, for example,

from He et al. [93].

at maximal coherence $\rho_{\rm bc}=1/2$, the ratio of the coherent and incoherent signals is approximately proportional to the number of molecules N, that is, fields produced by the coherent emitters add up in amplitude such that the

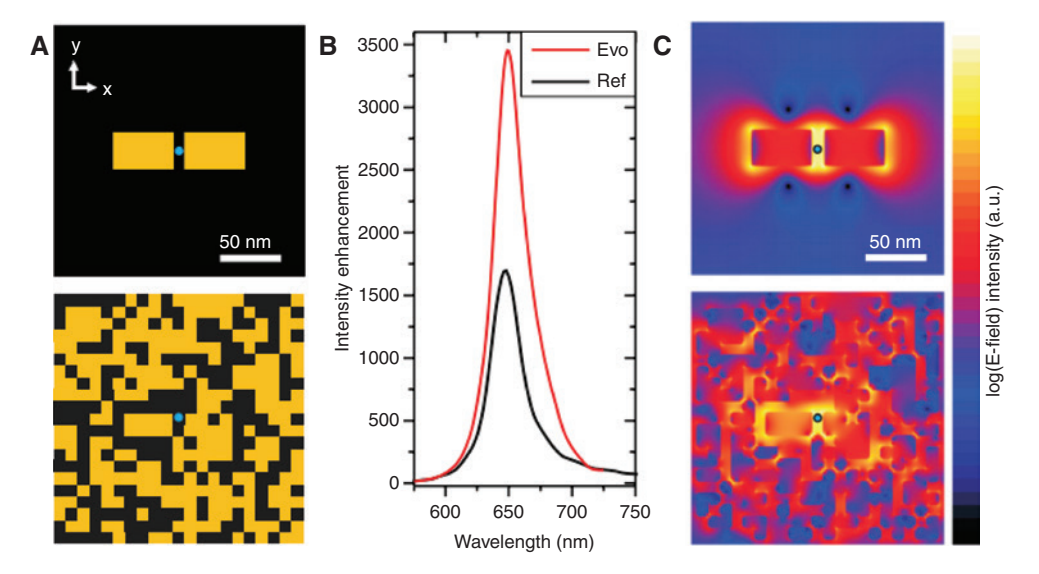


Figure 12: Optimal nanoantenna design.

Comparison between a resonant linear dipole nanoantenna with rectangular arms (A, top) and a matrix antenna nanostructure obtained with the evolutionary optimization (A, bottom). The scattering spectra in (B) are taken at the positions marked with blue dots in (A). (C) Near-field intensities at the two structures. Adapted from Feichtner et al. [129].

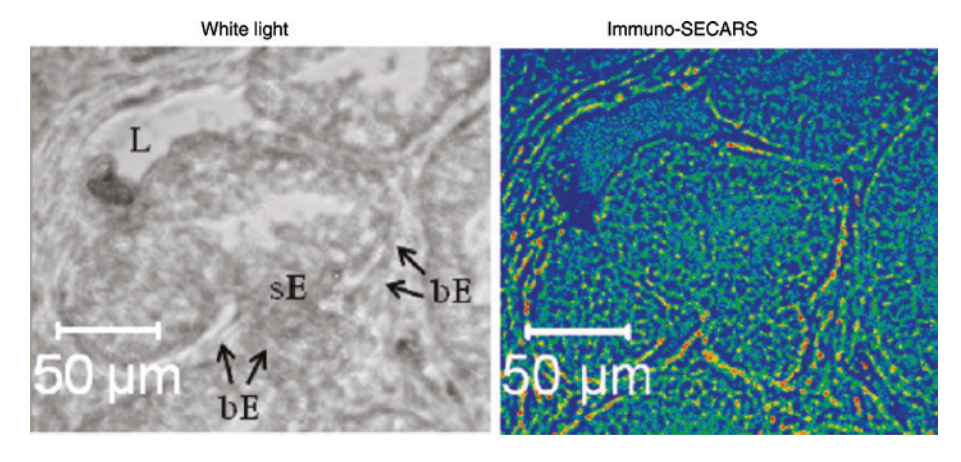


Figure 13: White light (left) and immune-SECARS (right) images of prostate tissue biopsies incubated with SERS-labeled p63 antibodies. The p63 protein is only abundant in the basal epithelium (bE, arrows) but not in the secretory epithelium (sE) or lumen (L) as shown by bright red spots in the immune-SECARS images. Adapted from Schlücker et al. [99].

intensity grows as the number of the coherent emitters squared, while the intensity of the incoherent emission is proportional to the number of emitters. In the limit of a single molecular vibrational oscillator, both signals will be equal and the coherence enhancement effect will be absent. In fact, the very term "molecular coherence" refers to a property of an ensemble and quantifies the relative "phasing" of ensemble members [121, 122]; the concept of coherence is unnecessary for the description of a truly single-oscillator process. Note that large molecules may consist of several, or many, (coupled) oscillators and, therefore, may exhibit the N2-type enhancement

mechanism, due to coherence among those multiple oscillators (within the single molecule). Coherence effects in multi-level quantum-mechanical systems, excited for example by pulsed laser fields, are of potential relevance to biological molecules. In a truly single-oscillator case however, the only remaining type of coherence, or phasing, is between the oscillator and an external reference, such as a pulsed laser field; this phasing may be used in the description of the heterodyne CARS or stimulated Raman techniques where this oscillator signal is coherently mixed with the external local oscillator field as described above.

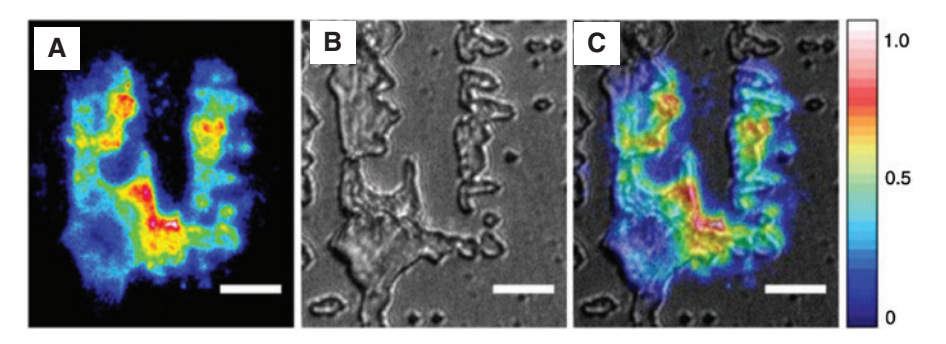


Figure 14: Wide-field SPP-based SECARS microscopy of lipid structures.
(A) SECARS, (B) transmission and (C) overlapped SECARS and transmission images of a thick aggregate of cholesteryl oleate. Scale bar, 20 μm. Adapted from Fast et al. [100].

4.6 Optimal nanostructure design

Next, we discuss strategies to optimize the nanostructured substrates to improve the SECARS efficiency. A previous discussion revealed the need for improving the near-field enhancement in the hot spots of the plasmonic nanostructures as well as the spatial overlap of the hot spot distributions of the pump, Stokes and probe fields. Fano resonances were used to improve the SECARS signals on plasmonic quadrumers [98]. These SECARS substrate designs may be further improved by varying the properties of the excitation laser fields and of the plasmonic substrates. For example, the properties of the plasmonic gold disk trimer were theoretically optimized to increase the SECARS signals by varying the incident laser excitation angle and using the double Fano resonance (Figure 11) [93]. The spatial near-field distributions of the pump, Stokes and probe showed hot spots in the same location in the trimer (Figure 11C). The good spatial overlap of the excitation fields and the suppressed absorption of the pump and Stokes placed in the dips of the double Fano resonance lead to the large predicted $\text{EF}_{\text{SECARS}/\text{CARS}}$ of $\sim\!10^{11}\text{,}$ which may be further increased to ~1013 by reducing the inter-particle gap size. This substrate geometry provides several control parameters to tune the properties of the plasmonic response.

Nanostructured substrates may be optimized in a more general way using a large parameter space and evolutionary algorithms. Metal NP array geometries were optimized using evolutionary algorithms to produce broadband plasmonic field enhancement [123], collocated resonances [124] and improved SERS signals [125] and for guiding light at the nanoscale [126–128]. Optical nanoantennas were also designed using a large parameter space evolutionary optimization [129]. Figure 12 shows optimization of the near-field intensity

enhancement in a checkerboard-type array of gold cubes using an evolutionary algorithm, leading to the discovery of a new-type split-ring-two-wire antenna geometry [129]. The optimized matrix antenna (Figure 12A, bottom) has stronger near-field enhancement than the previous optical nanoantenna designs that were developed using a deterministic approach such as the linear dipole (Figure 12B) [44], cross [119], bow tie [130, 131] and Yagi-Uda [132, 133] antennas. The evolutionary optimization resulted in nanoantenna structural features, which gave insight into new design strategies such as the coupling of the electric and magnetic resonances. These new strategies may be used to improve the design of the SECARS substrates. Deterministic and evolutionary optimizations are effective strategies to design nanostructures with the controllable spatiotemporal near-field distributions, which may be used for investigating ultrafast dynamics of single and few biomolecules.

4.7 Biological applications

Only a few biological applications of SECARS were shown so far in spite of more than 30 years since the first demonstration. Immuno-SECARS microscopy was demonstrated as the first application of the SECARS detection contrast for bio-imaging using immuno-based staining techniques [99]. Figure 13 shows white light (left) and immune-SECARS (right) images of prostate tissue biopsies labeled with p63-antibody-conjugated plasmonic NPs. The immuno-SECARS image shows an improved optical contrast providing a better localization of the p63 signals, fast imaging speed and suppression of the tissue autofluorescence background. In this biological imaging application, the SECARS signals were obtained from the Raman reporter labeling molecules conjugated to the plasmonic

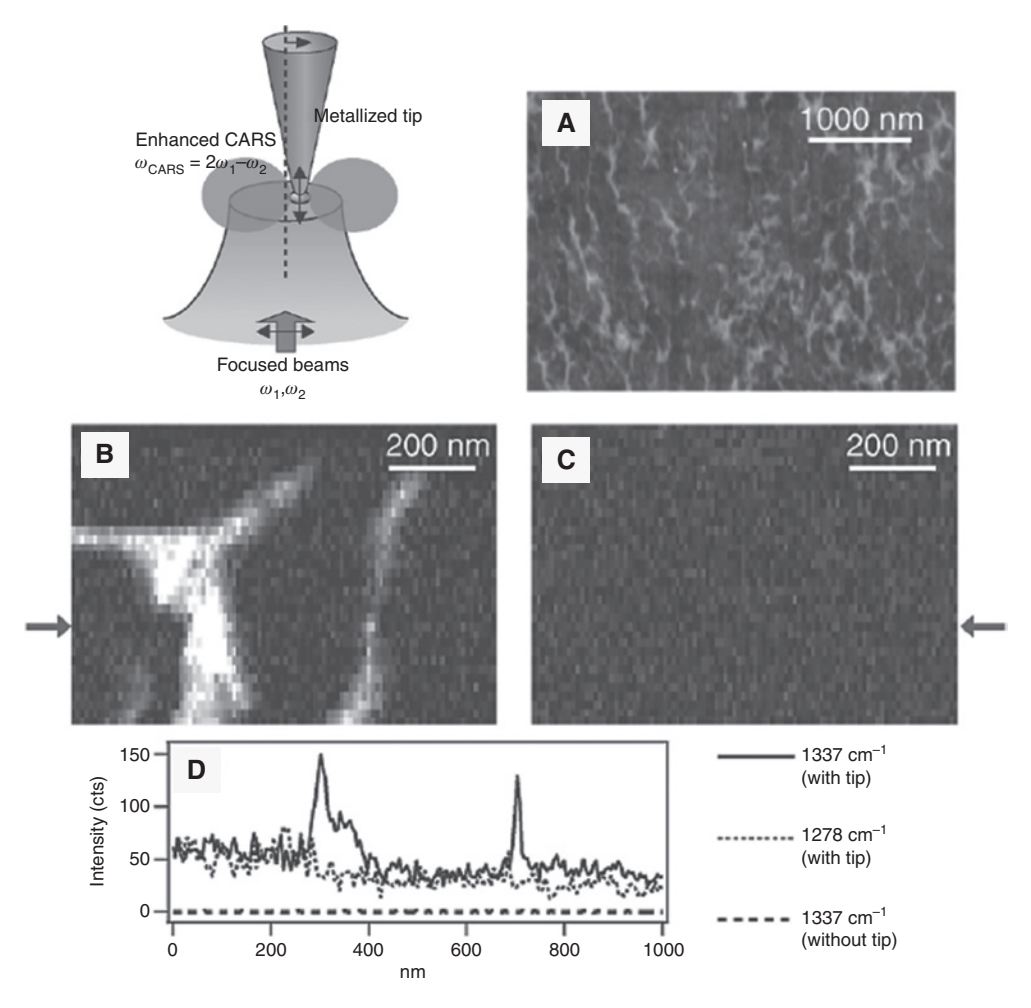


Figure 15: TECARS imaging of DNA network on a glass substrate using a metallized tip in a focused laser spot. (A) Topographic image of the DNA network. (B) On-resonance and (C) off-resonance TECARS images and (D) the corresponding cross-sectional line profiles indicated by arrows. Adapted from Ichimura et al. [101].

NPs interacting with the prostate tissues via the antibodies attached to NPs. The immuno-SECARS microscopy takes advantage of the target-specific nanoprobe staining and may be performed with several types of staining agents simultaneously in the multiplex spectroscopic mode. This may allow for simultaneous imaging of different cell targets. Future developments may be used to optimize the efficiency of this technique to improve the speed and signal enhancement. Various labels may be used to target specific biological processes. Label-free SECARS may also be used for nanoscale bio-imaging using scanning probe microscopy as discussed below.

Label-free SECARS application to bio-imaging was shown in the wide-field SECARS microscopy of lipid structures on a 30-nm-thick flat gold substrate [100]. This implementation of SECARS microscopy followed the original demonstration of SECARS [81], using evanescent fields of SPPs to generate the coherent Raman signals. Picosecond pump and Stokes laser beams were coupled to the gold surface via the Kretschmann configuration, and the reflected SECARS signal was detected in the epi-direction. High-contrast SECARS images of the aggregated cholesteryl oleate structures were obtained (Figure 14) using four orders of magnitude lower illumination density than in conventional CARS. This is advantageous for bio-imaging, where sample damage may easily occur due to overheating by intense ultrashort laser pulses. Future improvements of this technique may involve the suppression of the nonresonant FWM and two-photon photoluminescence backgrounds and weak CARS signals originating in the areas close to the lipid structures due to the back-coupling into the gold film (weak signals around the lipids in Figure 14). Promising future applications of SECARS to nanoscale imaging of cell membranes of whole cells in vivo may be achieved using this wide-field SECARS technique or by confining

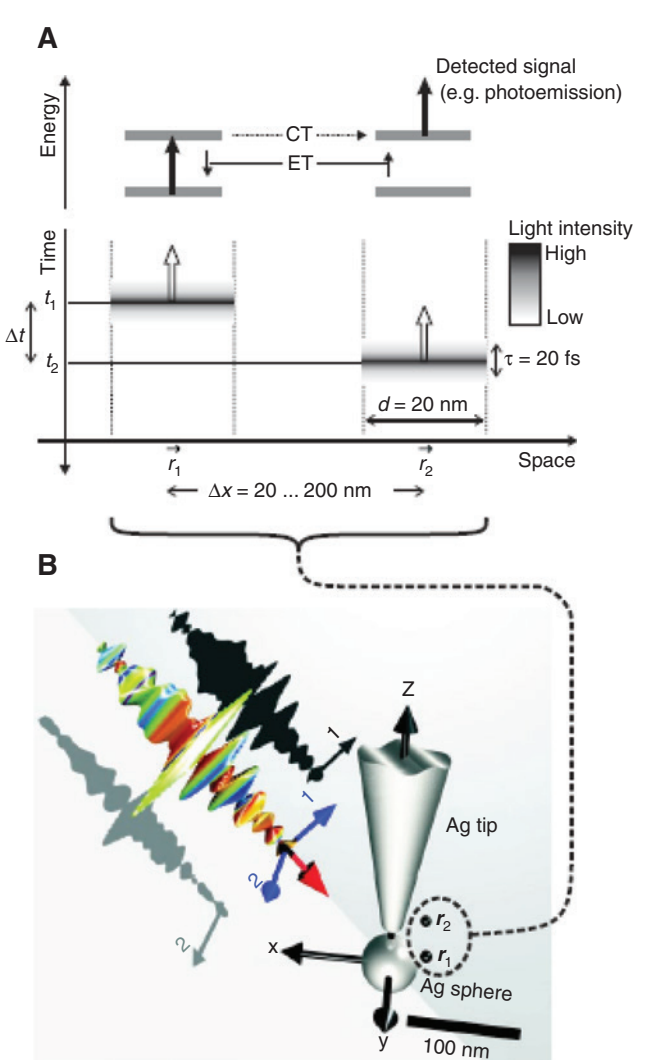


Figure 16: Near-field control.

(A) Schematic of ultrafast nanoscopic space-time-resolved spectroscopy. The objective is to study charge transfer (CT) or energy transfer (ET) ultrafast dynamics between two coupled quantum systems that are only a short distance apart with nanoscale spatial resolution and femtosecond temporal resolution. For example, the field first creates a local excitation at r_1 , and later the transferred excitation is detected at r_2 , for example, by photoelectron emission or SECARS. (B) The model nanostructure is illuminated by an optimized polarization-shaped femtosecond laser pulse which provides the designed spatiotemporal control of the electric fields to achieve the proposed objective. Adapted from Brixner et al. [134].

the excitation volume to the nanoscale using plasmonic scanning probes as described next.

4.8 TECARS

Similar to SERS bio-sensing, the TERS imaging of a small number of biomolecules with small Raman cross sections

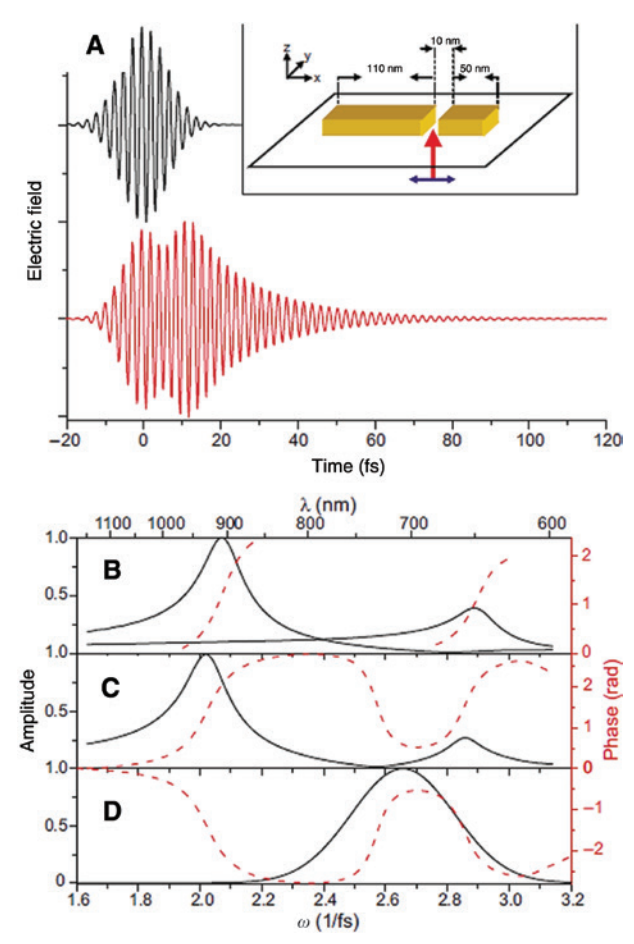


Figure 17: Control of optical nanoantenna response via phase compensation by laser pulse shaping.

(A) Time-dependent electric fields of the excitation source (black, top) and the corresponding near-field response (red, bottom) at the feed gap center of an asymmetric dipole antenna. (B) Impulsive spectral amplitudes (black solid lines) and phases (red dashed lines) of isolated 50- and 110-nm gold nanorods recorded at a point on the long axis of the rods, 5 nm from its end in air. (C) Impulsive spectrum (black solid line) and spectral phase (red dashed line) of the respective asymmetric antenna consisting of the two rods in (B), recorded at the center of the 10-nm gap. (D) Spectrum (black solid line) and phase (red dashed line) of a new source pulse with phase shaped as the opposite of the asymmetric antenna spectral phase shown in (C). Adapted from Huang et al. [135].

is challenging. In addition, the near-field enhancement of the tip is usually smaller than that of the nanostructured SERS substrates. Therefore, the combination of the surface enhancement of TERS and the coherence enhancement of CARS is promising for biological applications and has been demonstrated in several TECARS experiments [80, 88, 101–104].

The first TECARS imaging was shown on aggregated poly(dA-dT) DNA clusters with \sim 20-nm height and \sim 100-nm width and on DNA networks with \sim 2.5-nm

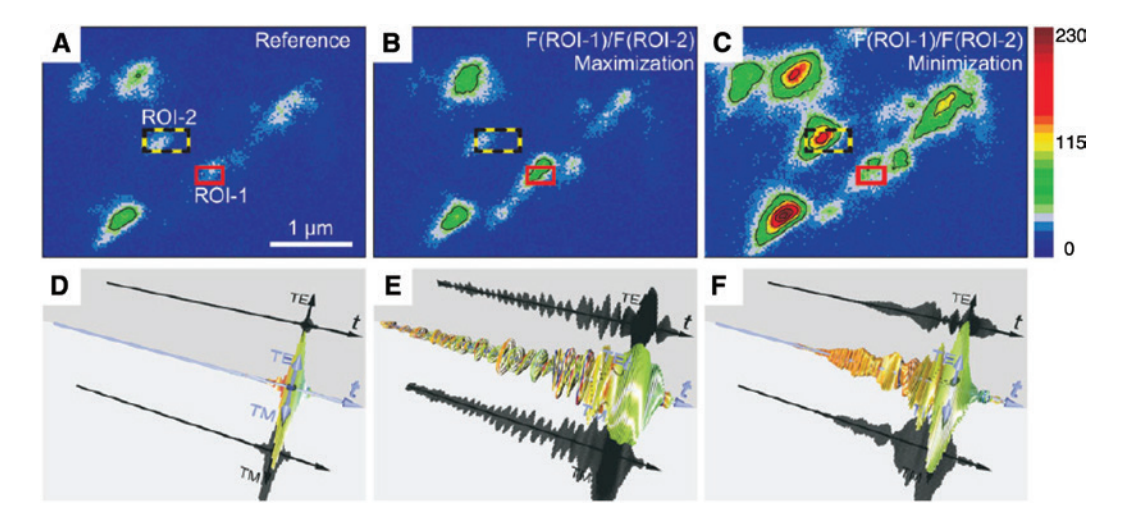


Figure 18: Near-field control of random plasmonic nanostructures by polarization laser pulse shaping. Contour plots of the photoelectron distributions on a plasmonic corrugated silver surface measured with PEEM are shown as obtained with unshaped transform-limited reference pulse (A and D) and adaptively optimized pulses maximizing (B and E) and minimizing (C and F) the ratio of the regions of interest ROI-1/ROI-2 shown by the dashed rectangles. (D-F) Corresponding optimal polarization-shaped laser pulses are shown in a quasi-3D representation with the time axis ranging from -1800 to 300 fs. Optimal pulses in (E) and (F) extend over much longer times and still lead to a "superenhancement" of the multiphoton photoemission signals. Adapted from Aeschlimann et al. [136].

height and up to few tens of nanometers width on a glass substrate using a silver-coated AFM probe and narrowband (~5 ps) laser excitation (Figure 15) [101]. Resonant excitation of the vibrational ring-breathing mode of adenine at ~1337 cm⁻¹ resulted in the high-contrast nanoscale bio-imaging (Figure 15B). However, the nonresonant excitation at ~1278 cm⁻¹ resulted in a poor contrast without significant structural features (Figure 15C). This first demonstration was followed by other TECARS experiments on DNA clusters [102], CNTs [88, 103] and polystyrene beads and mitochondria [104]. These results showed improvements in spatial resolution and signal strength compared to the conventional CARS microscopy. Broadband TECARS demonstrated a wide range of multiplex spectral imaging and ultrafast time-resolved measurement capabilities [103]. Radially polarized TECARS showed a sixfold increase of the signal compared to the linearly polarized TECARS [104]. However, in all these experiments, there were significant contributions of the nonresonant FWM and photoluminescence backgrounds from the tip which decreased the EFs and the imaging contrast. Future instrumentation improvements are envisioned that would optimize the signal-to-noise ratio by using the laser pulse shaping of the FAST CARS and by optimizing the tip geometry. The tip enhancement effect may be used not only for spectroscopic imaging but also for the manipulation of the near-field propagation dynamics in nano-plasmonic devices, which may also

be combined with near-field pulse shaping as discussed next.

4.9 Near-field control of nano-optical excitations

Near-field control by laser pulse shaping may be used to improve the performance of the nanoscale bio-imaging and to implement surface-enhanced FAST CARS. For example, the TECARS experiments described above may be improved by suppressing the nonresonant background using near-field pulse shaping in the analogy to the farfield FAST CARS. Also, the TECARS experiments may be designed to probe the ultrafast dynamics of nanoscale systems via the ultrafast nanoscopic space-time-resolved spectroscopy (Figure 16) [134]. Figure 16A shows the schematic of this technique, where a quantum system may be excited at the initial time t_1 at the location r_1 and may be later detected at time t_2 at location r_2 , with the ultrashort time and space intervals of a few femtoseconds and a few nanometers, respectively. This could be implemented by the control of the spatiotemporal near-field distribution in the vicinity of a plasmonic nanostructure, such as a silver TERS tip (Figure 16B). This scheme will allow obtaining molecular movies with unprecedented control in the ultrashort space-time limit. Various processes may be investigated using optically and electronically detected signals

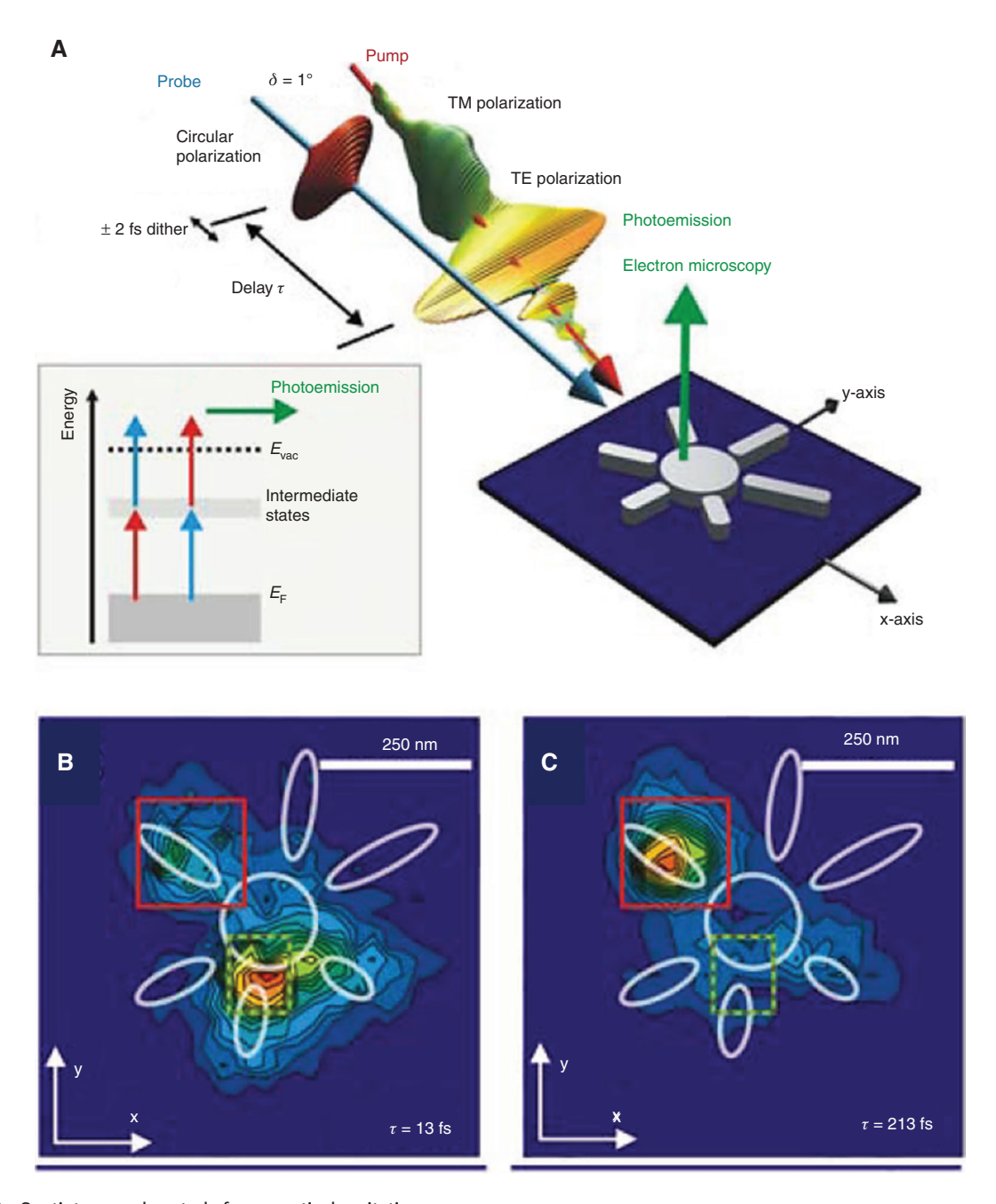


Figure 19: Spatiotemporal control of nano-optical excitations. (A) Experimental scheme shows polarization-shaped pump and circularly polarized probe laser pulses illuminating the plasmonic sunshaped nanostructure with an adjustable time delay τ . The inset shows two-photon excitation pathways for pump (red arrow) and probe interactions (blue arrow) that promote electrons from below the Fermi level $E_{\rm F}$ via intermediate states to above the vacuum energy $E_{\rm vac}$. Normalized cross-correlation emission patterns for the two different delays τ = 13 fs (B) and τ = 213 fs (C) show two different hot spots located at different positions and different times with ultrafast nanoscopic control. Adapted from Aeschlimann et al. [138].

such as photoemission electron microscopy (PEEM) and SECARS.

Laser pulse shaping may also be used to enhance the near-field excitation and signal collection efficiency in resonant optical nanoantennas [48, 135]. For example, the complex spectral phase profiles in coupled plasmonic

nanostructures such as asymmetric dipole nanoantennas lead to the stretching of the temporal near-field amplitude profiles and, therefore, to the lower nonlinear optical signals such as SECARS. Such complex phase profiles may be compensated by laser pulse shaping, leading to temporal pulse compression (Figure 17) [135].

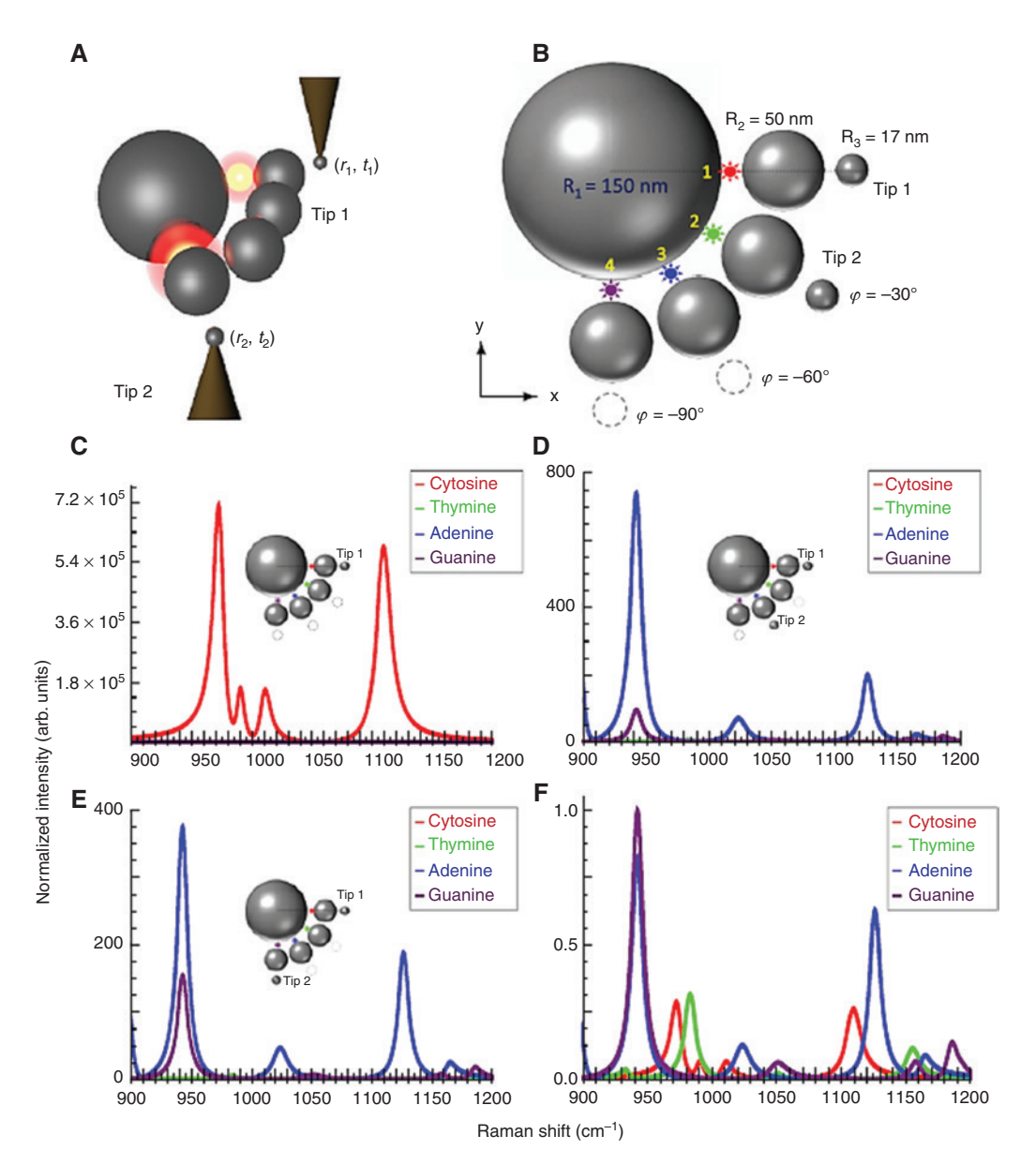


Figure 20: 2TECARS ultrafast nanoscopy using a plasmonic nanostructure made of self-similar nanolens antennas connected by a waveguide.

(A) Side view and (B) top view of the nanostructure and tips. The small nanospheres are attached to scanning probe microscope cantilevers, providing controlled subwavelength excitation and detection. Cytosine, thymine, adenine and guanine molecules are placed in the nearfield hot spots of the nanostructure in the gaps between the large- and medium-size spheres, labeled 1-4 and highlighted by red, green, blue and purple stars, respectively. The position of tip 1 is fixed. The position of tip 2 is varied between the values of the angle φ : no tip 2, -30°, -60° and -90°. The nanostructure is excited by x-polarized ultrashort laser pulses. The dynamics of near fields and 2TECARS signals are controlled by changing the position of tip 2 and by laser pulse shaping. Simulated 2TECARS nanospectra with different positions of tip 2 provide isolated Raman signals from the selected molecules: x-polarized without tip 2 (C) and y-polarized with tip 2 at -60° (D) and -90° (E). (C) and (D) primarily generate signals from cytosine and adenine molecules, respectively. (F) CARS spectra of the mixture of four DNA nucleobases without the nanostructure do not show any significant selectivity and reveal strong signals from all molecules. Tip 2 is used as a nanoscale control "knob" for the selective detection of molecules via 2TECARS. Adapted from Ballmann et al. [139].

Complex pulse shapes may be used to optimize the near-field response in complex nanostructures with long-lived coherences (Figure 18) [136]. For example, large enhancement of the multiphoton photoemission signals from a corrugated silver surface was obtained with complex polarization-shaped laser pulses (Figure 18B and C), resulting in the near-field "superenhancement". Complex local phase distributions may result in the decrease of the SECARS hot spots and may be optimized using this approach. Adaptive and analytic optimizations may be used to design optimal field shapes for specific targets [137].

Full spatiotemporal near-field control may be used to excite and probe different spatial locations with nanometer spatial resolution at different times with femtosecond temporal resolution. Figure 19 shows an example of the plasmonic sun-shaped nanostructure excited with optimally shaped pump and circularly polarized probe laser pulses to generate spatiotemporal near-field distributions with such desired properties. This ultrafast nanoscopic space-time near-field control may be used to probe charge and energy transfer dynamics in a variety of systems. PEEM or SECARS may be used as the signal detection method for probing the results of the near-field excitations. For example, plasmonic tips may be coupled to a nanostructure for performing near-field control and may be combined with pulse shaping and SECARS, as will be discussed next.

4.10 Ultrafast nanoscopy with multiple-tip TECARS: toward real space and time molecular movies

Simultaneous optimization of the nanostructure geometry and laser pulse shaping may be used to achieve the ultimate goal of recording molecular movies in real space and time. For example, we theoretically demonstrated a possibility of obtaining Raman signals from individual DNA nucleobases placed near a plasmonic nanostructure with femtosecond temporal and nanometer spatial resolutions (Figure 20). We used a plasmonic nanostructure made of self-similar nanolens antennas connected by a waveguide and placed cytosine, thymine, adenine and guanine molecules in the near-field hot spots of the gaps between the 50- and 150-nm spheres, labeled 1-4 and highlighted by red, green, blue and purple stars in Figure 20B, respectively. The nanostructure design was inspired by the plasmonic circuitry [135, 140] and the self-similar nanolens [141]. The position of tip 1 was fixed, forming an optical nanoantenna with the medium and large spheres oriented along the x axis. It generated a hot spot at position 1 for linearly polarized excitation. The near field at position 1 propagated along the waveguide formed on the surface of the large sphere, exciting other molecules in positions 2–4 at later times which were probed by tip 2. This forms the basis of the dual-TECARS (2TECARS) ultrafast nanoscopy [139], which takes advantage of the surface and coherence enhancement of the Raman signals and uses laser

pulse shaping to suppress the background from the undesired molecular signals in the analogy to FAST CARS. As a result, the specific molecular signals may be obtained from different spatial locations at different times, revealing the ultrafast plasmon propagation dynamics and energy or charge transfer within the coupled plasmonmolecular systems. These techniques may be applied to directly probe quantum energy and charge transport in photosynthetic systems [142–144].

5 Outlook

The future of quantum nano-biophotonics has been shaping in the form of new exciting technological developments and applications. Here, we described one of the best-of-both-worlds combinations of the coherence and SERS techniques, which provides nanoscale chemically specific and topographic information with ultrafast temporal resolution. Surface-enhanced FAST CARS offers a promising strategy to experimentally realize the predicted large EFs. Many other exciting ideas are on the horizon. Future experimental and theoretical developments need to address the discrepancies between the predicted and the observed surface-enhanced nonlinear optical signal enhancements.

Acknowledgments: This work was supported by the Office of Naval Research (grants N00014-16-1-3054 and N00014-16-1-2578), the Robert A. Welch Foundation (awards A1261 and A-1547), and the National Science Foundation (grant CHE-1609608).

References

- [1] Voronine DV, Altangerel N, Fry ES, et al. The dawn of quantum biophotonics. In: Al-Amri MD, El-Gomati M, Zubairy MS, eds. Optics in our time, Cham, Springer International Publishing, 2016, 147-76.
- [2] Minck RW, Terhune RW, Rado WG. Laser-stimulated Raman effect and resonant four-photon interactions in gases h2, d2, and ch4. Appl Phys Lett 1963:3:181-4.
- [3] Maker PD, Terhune RW. Study of optical effects due to an induced polarization third order in the electric field strength. Phys Rev 1965;137:A801-18.
- [4] Duncan MD, Reintjes J, Manuccia TJ. Scanning coherent anti-Stokes Raman microscope. Opt Lett 1982;7:350-2.
- [5] Zumbusch A, Holtom GR, Xie XS. Three-dimensional vibrational imaging by coherent anti-Stokes Raman scattering. Phys Rev Lett 1999;82:4142-5.
- Cheng J-X, Xie XS. Coherent Raman scattering microscopy. Hoboken, NJ, CRC Press, 2016.

- [7] Petrov GI, Arora R, Yakovlev VV, Wang X, Sokolov AV, Scully MO. Comparison of coherent and spontaneous Raman microspectroscopies for noninvasive detection of single bacterial endospores. Proc Natl Acad Sci 2007;104:7776-9.
- [8] Scully MO, Kattawar GW, Lucht RP, et al. FAST CARS: Engineering a laser spectroscopic technique for rapid identification of bacterial spores. Proc Natl Acad Sci 2002;99:10994-1001.
- [9] Pestov D, Murawski RK, Ariunbold GO, et al. Optimizing the laser-pulse configuration for coherent Raman spectroscopy. Science 2007;316:265-8.
- [10] Pestov D, Wang X, Ariunbold GO, et al. Single-shot detection of bacterial endospores via coherent Raman spectroscopy. Proc Natl Acad Sci 2008;105:422-7.
- [11] Shen Y, Voronine DV, Sokolov AV, Scully MO. A versatile setup using femtosecond adaptive spectroscopic techniques for coherent anti-Stokes Raman scattering. Rev Sci Instrum 2015;86:083107.
- [12] Gremlich H-U, Yan B. Infrared and Raman spectroscopy of biological materials. Hoboken, NJ, CRC Press, 2000.
- [13] Lewis IR, Edwards H. Handbook of Raman spectroscopy: from the research laboratory to the process line. Hoboken, NJ, CRC Press, 2001.
- [14] Schrader B. Infrared and Raman Spectroscopy: methods and applications. Chichester, UK, John Wiley & Sons, 2008.
- [15] Ghomi M. Applications of Raman spectroscopy to biology: from basic studies to disease diagnosis. Amsterdam, IOS Press,
- [16] Novotny L, Hecht B. Principles of nano-optics. Cambridge, Cambridge University Press, 2012.
- [17] Kneipp K, Moskovits M, Kneipp H. Surface-enhanced Raman scattering: physics and applications. Berlin, Springer Science & Business Media, 2006.
- [18] Ru EL, Etchegoin P. Principles of surface-enhanced Raman spectroscopy: and related plasmonic effects. Amsterdam, Elsevier, 2008.
- [19] Schlücker S. Surface enhanced Raman spectroscopy: analytical, biophysical and life science applications. Chichester, UK, John Wiley & Sons, 2011.
- [20] Kneipp K, Wang Y, Kneipp H, et al. Single molecule detection using surface-enhanced Raman scattering (SERS). Phys Rev Lett 1997;78:1667-70.
- [21] Jiang, Bosnick K, Maillard M, Brus L. Single molecule Raman spectroscopy at the junctions of large Ag nanocrystals. J Phys Chem B 2003;107:9964-72.
- [22] Steidtner J, Pettinger B. Tip-enhanced Raman spectroscopy and microscopy on single dye molecules with 15 nm resolution. Phys Rev Lett 2008;100:236101.
- [23] Luo Z, Loo BH, Peng A, Ma Y, Fu H, Yao J. Single-molecule surface-enhanced Raman scattering of fullerene C60. J Raman Spectrosc 2011;42:319-23.
- [24] Ru ECL, Etchegoin PG. Single-molecule surface-enhanced Raman spectroscopy. Annu Rev Phys Chem 2012;63:65-87.
- [25] Zrimsek AB, Wong NL, Van Duyne RP. Single molecule surface-enhanced Raman spectroscopy: a critical analysis of the bianalyte versus isotopologue proof. J Phys Chem C 2016:120:5133-4.
- [26] Deckert-Gaudig T, Deckert V. Tip-enhanced Raman scattering (TERS) and high-resolution bio nano-analysis – a comparison. Phys Chem Chem Phys 2010;12:12040-9.

- [27] Blum C, Schmid T, Opilik L, Weidmann S, Fagerer SR, Zenobi R. Understanding tip-enhanced Raman spectra of biological molecules: a combined Raman, SERS and TERS study. J Raman Spectrosc 2012:43:1895-904.
- [28] Schmid T, Opilik L, Blum C, Zenobi R. Nanoscale chemical imaging using tip-enhanced Raman spectroscopy: a critical review. Angew Chem Int Ed Engl 2013;52:5940-54.
- [29] Pozzi EA, Sonntag MD, Jiang N, Klingsporn JM, Hersam MC, Van Duyne RP. Tip-enhanced Raman imaging: an emergent tool for probing biology at the nanoscale, ACS Nano 2013:7:885-88.
- [30] Kumar N, Mignuzzi S, Su W, Roy D. Tip-enhanced Raman spectroscopy: principles and applications. EPJ Tech Instrum
- [31] Sharma G, Deckert-Gaudig T, Deckert V. Tip-enhanced Raman scattering – Targeting structure-specific surface characterization for biomedical samples. Adv Drug Deliv Rev 2015:89:42-56.
- [32] Tabatabaei M, McRae D, Lagugné-Labarthet F. Recent advances of plasmon-enhanced spectroscopy at bio-Interfaces. in Frontiers of Plasmon Enhanced Spectroscopy Volume 2, Vol. 1246 American Chemical Society, 2016:183-207.
- [33] Kurouski D. Advances of tip-enhanced Raman spectroscopy (TERS) in electrochemistry, biochemistry, and surface science. Vib Spectrosc 2017;91:3-15.
- [34] Stöckle RM, Suh YD, Deckert V, Zenobi R. Nanoscale chemical analysis by tip-enhanced Raman spectroscopy. Chem Phys Lett 2000;318:131-6.
- [35] Hayazawa N, Inouye Y, Sekkat Z, Kawata S. Metallized tip amplification of near-field Raman scattering. Opt Commun 2000;183:333-6.
- [36] Pettinger B, Picardi D, Schuster R, Ertl G. Surface enhanced Raman spectroscopy: towards single molecule spectroscopy. Electrochemistry 2000;68:942-9.
- [37] Anderson MS. Locally enhanced Raman spectroscopy with an atomic force microscope. Appl Phys Lett 2000;76:3130-2.
- [38] Liao M, Jiang S, Hu C, et al. Tip-enhanced Raman spectroscopic imaging of individual carbon nanotubes with subnanometer resolution. Nano Lett 2016;16:4040-6.
- [39] Zhang R, Zhang Y, Dong ZC, et al. Chemical mapping of a single molecule by plasmon-enhanced Raman scattering. Nature
- [40] Lin X-M, Deckert-Gaudig T, Singh P, et al. Direct base-to-base transitions in ssDNA revealed by tip-enhanced Raman Scattering. 2016; ArXiv160406598.
- [41] Flatau PJ, Fuller KA, Mackowski DW. Scattering by two spheres in contact: comparisons between discrete-dipole approximation and modal analysis. Appl Opt 1993;32:3302-5.
- [42] Romero I, Aizpurua J, Bryant GW, García De Abajo FJ. Plasmons in nearly touching metallic nanoparticles: singular response in the limit of touching dimers. Opt Express 2006;14:9988-99.
- [43] Halas NJ, Lal S, Chang W-S, Link S, Nordlander P. Plasmons in strongly coupled metallic nanostructures. Chem Rev 2011;111:3913-61.
- [44] Mühlschlegel P, Eisler H-J, Martin OJF, Hecht B, Pohl DW. Resonant optical antennas. Science 2005;308:1607-9.
- [45] Bharadwaj P, Deutsch B, Novotny L. Optical Antennas. Adv Opt Photonics 2009;1:438-83.
- [46] Novotny L, van Hulst N. Antennas for light. Nat Photonics 2011;5:83-90.
- [47] Biagioni P, Huang J-S, Hecht B. Nanoantennas for visible and infrared radiation. Rep Prog Phys 2012;75:024402.

- [48] Agio M, Alù A. Optical antennas. Cambridge, Cambridge University Press, 2013.
- [49] Pettinger B, Domke KF, Zhang D, Schuster R, Ertl G. Direct monitoring of plasmon resonances in a tip-surface gap of varying width. Phys Rev B 2007;76:113409.
- [50] Deckert-Gaudig T, Bailo E, Deckert V. Tip-enhanced Raman scattering (TERS) of oxidised glutathione on an ultraflat gold nanoplate. Phys Chem Chem Phys 2009;11:7360-2.
- [51] Stadler J, Oswald B, Schmid T, Zenobi R. Characterizing unusual metal substrates for gap-mode tip-enhanced Raman spectroscopy. J Raman Spectrosc 2013;44:227-33.
- [52] Wang H, Schultz ZD. The chemical origin of enhanced signals from tip-enhanced Raman detection of functionalized nanoparticles. Analyst 2013;138:3150-7.
- [53] Alajlan A, Voronine DV, Sinyukov AM, Zhang Z, Sokolov AV, Scully MO. Gap-mode enhancement on MoS2 probed by functionalized tip-enhanced Raman spectroscopy. Appl Phys Lett 2016;109:133106.
- [54] Zhang Y, Voronine DV, Qiu S, et al. Improving resolution in quantum subnanometre-gap tip-enhanced Raman nanoimaging. Sci Rep 2016;6:25788.
- [55] Zuloaga J, Prodan E, Nordlander P. Quantum description of the plasmon resonances of a nanoparticle dimer. Nano Lett 2009;9:887-91.
- [56] Mao L, Li Z, Wu B, Xu H. Effects of quantum tunneling in metal nanogap on surface-enhanced Raman scattering. Appl Phys Lett 2009;94:243102.
- [57] Esteban R, Borisov AG, Nordlander P, Aizpurua J. Bridging quantum and classical plasmonics with a quantum-corrected model. Nat Commun 2012;3:ncomms1806.
- [58] Savage KJ, Hawkeye MM, Esteban R, Borisov AG, Aizpurua J, Baumberg JJ. Revealing the quantum regime in tunnelling plasmonics. Nature 2012;491:574-7.
- [59] Scholl JA, García-Etxarri A, Koh AL, Dionne JA. Observation of quantum tunneling between two plasmonic nanoparticles. Nano Lett 2013;13:564-9.
- [60] Tan SF, Wu L, Yang JKW, Bai P, Bosman M, Nijhuis CA. Quantum plasmon resonances controlled by molecular tunnel junctions. Science 2014;343:1496-9.
- [61] Tame MS, McEnery KR, Özdemir ŞK, Lee J, Maier SA, Kim MS. Quantum plasmonics. Nat Phys 2013;9:329-40.
- [62] Zhu W, Crozier KB. Quantum mechanical limit to plasmonic enhancement as observed by surface-enhanced Raman scattering. Nat Commun 2014;5:ncomms6228.
- [63] Kravtsov V, Berweger S, Atkin JM, Raschke MB. Control of plasmon emission and dynamics at the transition from classical to quantum coupling. Nano Lett 2014;14:5270-5.
- [64] Ling X, Xie L, Fang Y, et al. Can graphene be used as a substrate for Raman enhancement? Nano Lett 2010;10:553-61.
- [65] Ling X, Fang W, Lee Y-H, et al. Raman enhancement effect on two-dimensional layered materials: graphene, h-BN and MoS2. Nano Lett 2014;14:3033-40.
- [66] Sun L, Hu H, Zhan D, et al. Plasma modified MoS2 nanoflakes for surface enhanced Raman scattering. Small 2014;10:1090-5.
- [67] Campion A, Ivanecky JE, Child CM, Foster M. On the mechanism of chemical enhancement in surface-enhanced Raman scattering. J Am Chem Soc 1995;117:11807-8.
- [68] Otto A. The 'chemical' (electronic) contribution to surfaceenhanced Raman scattering. J Raman Spectrosc 2005:36: 497-509.

- [69] Fromm DP, Sundaramurthy A, Kinkhabwala A, Schuck PJ, Kino GS, Moerner WE. Exploring the chemical enhancement for surface-enhanced Raman scattering with Au bowtie nanoantennas. J Chem Phys 2006:124:061101.
- [70] Wu D-Y, Liu X-M, Duan S, et al. Chemical enhancement effects in SERS spectra: a quantum chemical study of pyridine interacting with copper, silver, gold and platinum metals. J Phys Chem C 2008:112:4195-204.
- [71] Lombardi JR, Birke RL. A unified view of surface-enhanced Raman scattering, Acc Chem Res. 2009:42:734-42.
- [72] Moskovits M. Persistent misconceptions regarding SERS. Phys Chem Chem Phys 2013;15:5301-11.
- Valley N, Greeneltch N, Van Duyne RP, Schatz GC. A look at [73] the origin and magnitude of the chemical contribution to the enhancement mechanism of surface-enhanced Raman spectroscopy (SERS): theory and experiment. J Phys Chem Lett 2013;4:2599-604.
- [74] Lis D, Cecchet F. Localized surface plasmon resonances in nanostructures to enhance nonlinear vibrational spectroscopies: towards an astonishing molecular sensitivity. Beilstein J Nanotechnol 2014;5:2275-292.
- [75] Frontiera RR, Henry A-I, Gruenke NL, Van Duyne RP. Surfaceenhanced femtosecond stimulated Raman spectroscopy. J Phys Chem Lett 2011;2:1199-203.
- [76] Keller EL, Brandt NC, Cassabaum AA, Frontiera RR. Ultrafast surface-enhanced Raman spectroscopy. Analyst 2015;140:4922-31.
- [77] Gruenke NL, Cardinal MF, McAnally MO, Frontiera RR, Schatz GC, Duyne RPV. Ultrafast and nonlinear surface-enhanced Raman spectroscopy. Chem Soc Rev 2016;45:2263-90.
- [78] Chulhai DV, Hu Z, Moore JE, Chen X, Jensen L. Theory of linear and nonlinear surface-enhanced vibrational spectroscopies. Annu Rev Phys Chem 2016;67:541-64.
- [79] Deka G, Sun C-K, Fujita K, Chu S-W. Nonlinear plasmonic imaging techniques and their biological applications. Nanophotonics 2016:6:31-49.
- [80] Kawata S, Ichimura T, Taguchi A, Kumamoto Y. Nano-Raman scattering microscopy: resolution and enhancement. Chem Rev 2017;117:4983-5001.
- [81] Chen CK, de Castro ARB, Shen YR, DeMartini F. Surface coherent anti-Stokes Raman spectroscopy. Phys Rev Lett 1979;43:946-9.
- [82] Liang EJ, Weippert A, Funk J-M, Materny A, Kiefer W. Experimental observation of surface-enhanced coherent anti-Stokes Raman scattering. Chem Phys Lett 1994;227:
- [83] Chew H, Wang D-S, Kerker M. Surface enhancement of coherent anti-Stokes Raman scattering by colloidal spheres. JOSA B 1984:1:56-66.
- [84] Parkhill JA, Rappoport D, Aspuru-Guzik A. Modeling coherent anti-Stokes Raman scattering with time-dependent density functional theory: vacuum and surface enhancement. J Phys Chem Lett 2011;2:1849-54.
- [85] Hua X, Voronine DV, Ballmann CW, Sinyukov AM, Sokolov AV, Scully MO. Nature of surface-enhanced coherent Raman scattering. Phys Rev A 2014;89:043841.
- [86] Ichimura T, Hayazawa N, Hashimoto M, Inouye Y, Kawata S. Local enhancement of coherent anti-Stokes Raman scattering by isolated gold nanoparticles. J Raman Spectrosc 2003;34:651-4.

- [87] Namboodiri V, Namboodiri M, Diaz GIC, Oppermann M, Flachenecker G, Materny A. Surface-enhanced femtosecond CARS spectroscopy (SE-CARS) on pyridine. Vib Spectrosc 2011:56:9-12.
- [88] Hayazawa N, Ichimura T, Hashimoto M, Inouye Y, Kawata S. Amplification of coherent anti-Stokes Raman scattering by a metallic nanostructure for a high resolution vibration microscopy. J Appl Phys 2004;95:2676-81.
- [89] Crampton KT, Zeytunyan A, Fast AS, et al. Ultrafast coherent Raman scattering at plasmonic nanojunctions. J Phys Chem C 2016;120:20943-53.
- [90] Addison CJ, Konorov SO, Brolo AG, Blades MW, Turner RFB. Tuning gold nanoparticle self-assembly for optimum coherent anti-Stokes Raman scattering and second harmonic generation response. J Phys Chem C 2009;113:3586-92.
- [91] Steuwe C, Kaminski CF, Baumberg JJ, Mahajan S. Surface enhanced coherent anti-Stokes Raman scattering on nanostructured gold surfaces. Nano Lett 2011;11:5339-43.
- [92] Nevels R, Welch GR, Cremer PS, et al. Figuration and detection of single molecules. Mol Phys 2012;110:1993-2000.
- [93] He J, Fan C, Ding P, Zhu S, Liang E. Near-field engineering of Fano resonances in a plasmonic assembly for maximizing CARS enhancements. Sci Rep 2016;6:20777.
- [94] Voronine DV, Sinyukov AM, Hua X, et al. Time-resolved surface-enhanced coherent sensing of nanoscale molecular complexes. Sci Rep 2012;2:891.
- [95] Yampolsky S, Fishman DA, Dey S, et al. Seeing a single molecule vibrate through time-resolved coherent anti-Stokes Raman scattering. Nat Photonics 2014;8:650-6.
- [96] Voronine DV, Sinyukov AM, Hua X, et al. Complex line shapes in surface-enhanced coherent Raman spectroscopy. J Mod Opt 2015;62:90-6.
- [97] Koo T-W, Chan S, Berlin AA. Single-molecule detection of biomolecules by surface-enhanced coherent anti-Stokes Raman scattering. Opt Lett 2005;30:1024-6.
- [98] Zhang Y, Zhen Y-R, Neumann O, Day JK, Nordlander P, Halas NJ. Coherent anti-Stokes Raman scattering with single-molecule sensitivity using a plasmonic Fano resonance. Nat Commun 2014;5:4424.
- [99] Schlücker S, Salehi M, Bergner G, et al. Immuno-surfaceenhanced coherent anti-Stokes Raman scattering microscopy: immunohistochemistry with target-specific metallic nanoprobes and nonlinear Raman microscopy. Anal Chem 2011;83:7081-5.
- [100] Fast A, Kenison JP, Syme CD, Potma EO. Surface-enhanced coherent anti-Stokes Raman imaging of lipids. Appl Opt 2016;55:5994-6000.
- [101] Ichimura T, Hayazawa N, Hashimoto M, Inouye Y, Kawata S. Tip-enhanced coherent anti-Stokes Raman scattering for vibrational nanoimaging. Phys Rev Lett 2004;92:220801.
- [102] Ichimura T, Hayazawa N, Hashimoto M, Inouye Y, Kawata S. Application of tip-enhanced microscopy for nonlinear Raman spectroscopy. Appl Phys Lett 2004;84:1768-70.
- [103] Furusawa K, Hayazawa N, Catalan FC, Okamoto T, Kawata S. Tip-enhanced broadband CARS spectroscopy and imaging using a photonic crystal fiber based broadband light source. J Raman Spectrosc 2012;43:656-61.
- [104] Lin J, Er KZJ, Zheng W, Huang Z. Radially polarized tipenhanced near-field coherent anti-Stokes Raman scattering microscopy for vibrational nano-imaging. Appl Phys Lett 2013;103:083705.

- [105] Le Ru EC, Blackie E, Meyer M, Etchegoin PG. Surface enhanced Raman scattering enhancement factors: a comprehensive study. J Phys Chem C 2007;111:13794-803.
- [106] Oron D, Dudovich N, Silberberg Y. Single-pulse phasecontrast nonlinear Raman spectroscopy. Phys Rev Lett 2002;89:273001.
- [107] Potma EO, Evans CL, Xie XS. Heterodyne coherent anti-Stokes Raman scattering (CARS) imaging. Opt Lett 2006;31:241-3.
- [108] Lim S-H, Caster AG, Nicolet O, Leone SR. Chemical imaging by single pulse interferometric coherent anti-stokes Raman scattering microscopy. J Phys Chem B 2006;110:5196-204.
- [109] Müller C, Buckup T, von Vacano B, Motzkus M. Heterodyne single-beam CARS microscopy. J Raman Spectrosc 2009;40:809-16.
- [110] Camp CH, Lee YJ, Heddleston JM, et al. High-speed coherent Raman fingerprint imaging of biological tissues. Nat Photonics 2014:8:627-34.
- [111] Wang X, Wang K, Welch GR, Sokolov AV. Heterodyne coherent anti-Stokes Raman scattering by the phase control of its intrinsic background. Phys Rev A 2011;84:021801.
- [112] Babin SA, Churkin DV, Kablukov SI, Podivilov EV. Raman gain saturation at high pump and Stokes powers. Opt Express 2005;13:6079-84.
- [113] Scalora M, Vincenti MA, de Ceglia D, Grande M, Haus JW. Spontaneous and stimulated Raman scattering near metal nanostructures in the ultrafast, high-intensity regime. JOSA B 2013;30:2634-9.
- [114] Danckwerts M, Novotny L. Optical frequency mixing at coupled gold nanoparticles. Phys Rev Lett 2007;98:026104.
- [115] Wang Y, Lin C-Y, Nikolaenko A, Raghunathan V, Potma EO. Fourwave mixing microscopy of nanostructures. Adv Opt Photonics 2011;3:1-52.
- [116] Poutrina E, Ciracì C, Gauthier DJ, Smith DR. Enhancing fourwave-mixing processes by nanowire arrays coupled to a gold film. Opt Express 2012;20:11005-13.
- [117] Zhang Y, Wen F, Zhen Y-R, Nordlander P, Halas NJ. Coherent Fano resonances in a plasmonic nanocluster enhance optical four-wave mixing. Proc Natl Acad Sci 2013;110:9215-9.
- [118] Wang J, Zhang J, Tian Y, et al. Theoretical investigation of a multi-resonance plasmonic substrate for enhanced coherent anti-Stokes Raman scattering. Opt Express 2017;25:497-507.
- [119] Biagioni P, Huang JS, Duò L, Finazzi M, Hecht B. Cross resonant optical antenna. Phys Rev Lett 2009;102:256801.
- [120] Yu N, Genevet P, Kats MA, et al. Light propagation with phase discontinuities: generalized laws of reflection and refraction. Science 2011;334:333-7.
- [121] Sokolov AV, Shverdin MY, Walker DR, et al. Generation and control of femtosecond pulses by molecular modulation. J Mod Opt 2005;52:285-304.
- [122] Pestov D, Ariunbold GO, Wang X, et al. Coherent versus incoherent Raman scattering: molecular coherence excitation and measurement. Opt Lett 2007;32:1725-7.
- [123] Forestiere C, Donelli M, Walsh GF, Zeni E, Miano G, Negro LD. Particle-swarm optimization of broadband nanoplasmonic arrays. Opt Lett 2010;35:133-5.
- [124] Ginzburg P, Berkovitch N, Nevet A, Shor I, Orenstein M. Resonances on-demand for plasmonic nano-particles. Nano Lett 2011;11:2329-33.
- [125] Forestiere C, Pasquale AJ, Capretti A, et al. Genetically engineered plasmonic nanoarrays. Nano Lett 2012;12:2037-44.

- [126] Sukharev M, Seideman T. Coherent control approaches to light guidance in the nanoscale. J Chem Phys 2006;124:144707.
- Sukharev M, Seideman T. Phase and polarization control as a route to plasmonic nanodevices. Nano Lett 2006;6:715-9.
- [128] Yelk J, Sukharev M, Seideman T. Optimal design of nanoplasmonic materials using genetic algorithms as a multiparameter optimization tool. J Chem Phys 2008;129:064706.
- [129] Feichtner T, Selig O, Kiunke M, Hecht B. Evolutionary optimization of optical antennas. Phys Rev Lett 2012;109:127701.
- [130] Schuck Pl. Fromm DP. Sundaramurthy A. Kino GS. Moerner WE. Improving the mismatch between light and nanoscale objects with gold bowtie nanoantennas. Phys Rev Lett 2005;94:017402.
- [131] Farahani JN, Pohl DW, Eisler H-J, Hecht B. Single quantum dot coupled to a scanning optical antenna: a tunable superemitter. Phys Rev Lett 2005;95:017402.
- [132] Taminiau TH, Stefani FD, van Hulst NF, Enhanced directional excitation and emission of single emitters by a nano-optical Yagi-Uda antenna. Opt Express 2008;16:10858-66.
- [133] Curto AG, Volpe G, Taminiau TH, Kreuzer MP, Quidant R, van Hulst NF. Unidirectional emission of a quantum dot coupled to a nanoantenna. Science 2010;329:930-3.
- [134] Brixner T, García de Abajo FJ, Schneider J, Pfeiffer W. Nanoscopic ultrafast space-time-resolved spectroscopy. Phys Rev Lett 2005;95:093901.
- [135] Huang JS, Voronine DV, Tuchscherer P, Brixner T, Hecht B. Deterministic spatiotemporal control of optical fields in nanoantennas and plasmonic circuits. Phys Rev B 2009;79:195441.

- [136] Aeschlimann M, Brixner T, Cunovic S, et al. Nano-optical control of hot-spot field superenhancement on a corrugated silver surface. IEEE J Sel Top Quantum Electron 2012;18:275-82.
- [137] Tuchscherer P, Rewitz C, Voronine DV, de Abajo FJG, Pfeiffer W, Brixner T. Analytic coherent control of plasmon propagation in nanostructures. Opt Express 2009;17:14235-59.
- [138] Aeschlimann M, Bauerb M, Bayera D, et al. Spatiotemporal control of nanooptical excitations. Proc Natl Acad Sci 2010;107:5329-33.
- [139] Ballmann CW. Cao B. Sinvukov AM. Sokolov AV. Voronine DV. Dual-tip-enhanced ultrafast CARS nanoscopy. New J Phys 2014;16:083004.
- [140] Huang J-S, Feichtner T, Biagioni P, Hecht B. Impedance matching and emission properties of nanoantennas in an optical nanocircuit. Nano Lett 2009;9:1897-902.
- [141] Li K. Stockman MI, Bergman DI, Self-similar chain of metal nanospheres as an efficient nanolens. Phys Rev Lett 2003;91:227402.
- [142] Engel GS, Calhoun TR, Read EL, et al. Evidence for wavelike energy transfer through quantum coherence in photosynthetic systems. Nature 2007;446:782-6.
- [143] Panitchayangkoon G, Voronine DV, Abramavicius D, et al. Direct evidence of quantum transport in photosynthetic lightharvesting complexes. Proc Natl Acad Sci 2011;108:20908-12.
- [144] Dorfman KE, Voronine DV, Mukamel S, Scully MO. Photosynthetic reaction center as a quantum heat engine. Proc Natl Acad Sci 2013;110:2746-51.